VILNIUS UNIVERSITY
LIFE SCIENCES CENTER

Guoda Gasauskaitė

Photoactive Biopolymer-C_{60} Nanocomposite Films for Biofouling Resistance

Master's Thesis

Molecular Biotechnology study program

Thesis supervisor
Dr. Wanessa CMA Melo

Consultant
Dr. María Belén Montero Rodríguez

Thesis completed at
Center for Physical Sciences and Technology (FTMC)

Contents

Abbreviations

aPDT – antimicrobial photodynamic therapy

BHI – brain heart infusion broth

C_{60} – fullerene C_{60}

CCD – charge-coupled device

CFU – colony-forming unit

CITENI – Research Center for Naval and Industrial Technologies

DMF – N, N-dimethylformamide

DPA – 9,10-dimethylanthracene

DSC – differential scanning calorimetry

EPS – extracellular polymeric substance

FTMC – Center for Physical Sciences and Technology

HAI – healthcare-associated infection

LED – light-emitting diode

LSC – Life Sciences Center

MDR – multidrug-resistant

MRSA – methicillin-resistant Staphylococcus aureus

OD – optical density

PBS – phosphate-buffered saline

PEG – polyethylene glycol

PHBV – poly(3-hydroxybutyrate-co-3-hydroxyvalerate)

PLA – poly (lactic acid)

PS – photosensitizer

ROS – reactive oxygen species

SE – secondary electron

SEM – scanning electron microscopy

Ta – tantalum

TBO – toluidine blue O

UV – ultraviolet

UV–Vis – ultraviolet–visible spectroscopy

VU – Vilnius University

Xc – degree of crystallinity

XRD – X-ray diffraction

Introduction

Hospital-acquired infections (HAIs) remain a major global healthcare problem, contributing to prolonged hospitalisation, increased treatment costs, and higher patient morbidity and mortality rates. Biofilms are estimated to be associated with approximately 60–70% of nosocomial infections, particularly those involving indwelling medical devices (Bouhrour et al., 2024). They are structured microbial communities embedded in a self-produced extracellular polymeric matrix that protects cells from antimicrobial agents, host immune response, and environmental stressors (Flemming et al., 2016). *Staphylococcus aureus*, especially methicillin-resistant *S. aureus* (MRSA), is a major contributor to HAIs because of its antibiotic resistance, clinical persistence, and ability to colonise surfaces involved in the formation of biofilms (Otto, 2018). Thus, new strategies are needed to target biofilm-associated microorganisms, and antimicrobial photodynamic therapy (aPDT) has emerged as a promising approach.

Antimicrobial photodynamic therapy (aPDT) relies on photosensitizers that generate reactive oxygen species (ROS) under illumination in the presence of oxygen, causing oxidative damage to microbial cells (Hamblin, 2016). These ROS damage multiple cellular targets simultaneously, reducing the likelihood of resistance development and enabling spatial control of antimicrobial activity (Tegos et al., 2005). Fullerene C_{60} is an attractive photosensitizer because of its photostability, long-lived excited states, and ability to generate ROS through both Type I and Type II photochemical pathways (Heredia et al., 2022). However, its hydrophobicity and tendency to aggregate in solutions limit its direct application (Heredia et al., 2022). Incorporation into polymer matrices can improve its dispersion, reduce leaching, and support the development of stable photoactive surfaces. Polymer combinations with C_{60} offer a route toward scalable, solvent-free fabrication of photoactive antimicrobial films using thermomechanical processing (Soon et al., 2013).

Despite the potential of C_{60}-based aPDT, its use in stable antimicrobial surfaces is still limited by poor fullerene dispersion, aggregation, and the lack of scalable methods for producing solid photoactive films. Therefore, this thesis addresses the need for non-leaching, light-activated antimicrobial surfaces by incorporating C_{60} into biopolymer matrices through thermomechanical processing. This work focuses on PLA-, PHBV-, and chitosan-based C_{60} composite films and evaluates their structure, ROS generation, and antibacterial activity against S. aureus. In this way, this thesis examines whether thermomechanically processed biopolymer–C_{60} films can provide a basis for biofouling-resistant photoactive surfaces.

Work aim and objectives

Aim:

To fabricate biopolymer–fullerene composite films and evaluate their antimicrobial photodynamic activity against *Staphylococcus aureus*

Objectives:

1. To prepare PLA-, PHBV-, and chitosan-based films containing fullerene C_{60}
2. To characterize the structure and C_{60} incorporation in the composite films
3. To evaluate ROS generation by the C_{60}-containing films under light irradiation
4. To assess the antimicrobial photodynamic activity of the composite films against *Staphylococcus aureus*

1. Literature review

1.1. Introduction to Biofilms and Their Clinical Relevance

1.1.1. What are biofilms?

Biofilms are structured communities of microorganisms that attach to surfaces and become embedded within a self-produced extracellular polymeric substance (EPS) matrix (Flemming et al., 2016). The EPS matrix mainly comprises polysaccharides, proteins, extracellular DNA, and lipids, and is essential for maintaining biofilm structure and function. By providing mechanical stability and protection, the matrix helps resident cells withstand environmental stress, host immune responses, antimicrobial exposure, and physical disruption (Almatroudi, 2025).

1.1.2. Biofilm formation

Biofilm formation is a complex and highly regulated process in which microorganisms transition from free-living (planktonic) cells to surface-associated multicellular communities. This process involves five stages: reversible attachment, irreversible attachment, early maturation, late maturation, and dispersion (Tolker-Nielsen, 2015). A schematic overview of this developmental process is shown in Figure 1.

The first stage of biofilm formation is the reversible adhesion of planktonic cells to surfaces. This initial contact is regulated by physicochemical interactions between microorganisms and surfaces (Sauer et al., 2023). Long-range forces, such as van der Waals forces, electrostatic forces, and hydrophobic effects, help position cells near the surface. However, short-range interactions, including hydrogen bonding and other adhesive interactions, stabilise this contact (Sauer et al., 2023). At this stage, attachment is weak, and cells can be relatively easily removed or inactivated by antimicrobial agents (X. Wang et al., 2023).

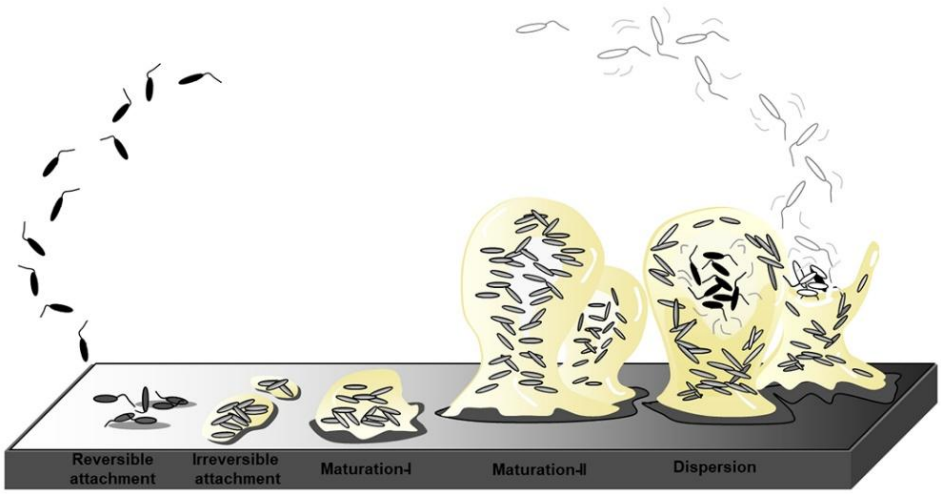

Figure 1. Developmental stages of microbial biofilm formation. This schematic illustrates biofilm development in *Pseudomonas aeruginosa*, including reversible attachment, irreversible attachment, early maturation (maturation I), late maturation (3D architecture with matrix-enclosed structures and maturation II), and active dispersion of the biofilm. Adapted from (Sauer et al., 2023)

In the second stage, attachment becomes permanent, and microbial cells begin to produce EPS, which forms the structural basis of the biofilm matrix. EPS may account for 50%–90% of the organic carbon in a biofilm (Donlan, 2002). EPS components create a hydrated, gel-like matrix that promotes adhesion, cohesion, and retention on surfaces (Flemming et al., 2016). The matrix also provides protection to cells against a range of external stresses, including desiccation, UV radiation, predation, host immune responses, and antimicrobial exposure. The close spatial arrangement of cells within the matrix facilitates horizontal gene transfer between microorganisms, thereby enabling the spread of antimicrobial resistance determinants (Almatroudi, 2025).

Following irreversible attachment, the maturation phase commences. During this stage, cells start to proliferate, and the biofilm begins to grow, giving rise to microcolonies and forming a complex three-dimensional structure (X. Wang et al., 2023). Altered metabolic activity allows cells to evade antimicrobial agent uptake or evade their effects (Jo et al., 2022). Thus, even if most of the biofilm is removed from the surface, the remaining persister and dormant cells will quickly proliferate and renew biofilm formation.

The final stage of the biofilm life cycle is dispersion, during which cells are released from mature biofilms and can colonise new surfaces (Sauer et al., 2023). Dispersion plays an important role in the spread of biofilm-related contamination and infection, as released cells can initiate biofilm formation at new sites and contribute to persistent or recurrent diseases (Sharma et al., 2023).

1.1.3. Biofilms in healthcare settings and the importance of *Staphylococcus aureus*

Biofilms are a major concern in healthcare settings because they act as persistent reservoirs of healthcare-associated infections (HAI). According to a 2024 report by the European Centre for Disease Prevention and Control, approximately 4.3 million patients in the EU/EEA acquire at least one HAI during hospitalisation each year (Point Prevalence Survey of Healthcare-Associated Infections and Antimicrobial Use in European Acute Care Hospitals – 2022-2023, 2024). These infections emerge ≥ 48 h after admission, leading to increased morbidity and mortality, extended hospital stays, and a significant burden on healthcare systems (Bouhrour et al., 2024). Biofilms play a direct role in this issue by establishing themselves, persisting, and continuously releasing microorganisms from both patient-associated and environmental sources.

In clinical settings, biofilms form on biotic and abiotic surfaces, and implanted and indwelling medical devices are particularly vulnerable (Figure 2) (Lindsay & von Holy, 2006). Device-associated biofilms are implicated in approximately 60%-70% of nosocomial infections, affecting catheters, prostheses, pacemakers, endotracheal tubes, contact lenses, and reusable semi-critical instruments (Bouhrour et al., 2024). These devices favour biofilm persistence by providing stable surfaces, prolonged exposure, and a continuous nutrient supply from body fluids, making infections difficult to eradicate and often requiring device removal or replacement (De-la-Pinta et al., 2019; Ul Haq et al., 2024).

High-touch environmental surfaces also act as biofilm reservoirs (Lindsay & von Holy, 2006). Dry-surface biofilms are especially relevant because they tolerate routine cleaning and disinfection (Ledwoch et al., 2018). A multicentre UK study detected multispecies dry biofilms on 95% of disinfected high-touch items, with 58% positive for MRSA (Ledwoch et al., 2018).

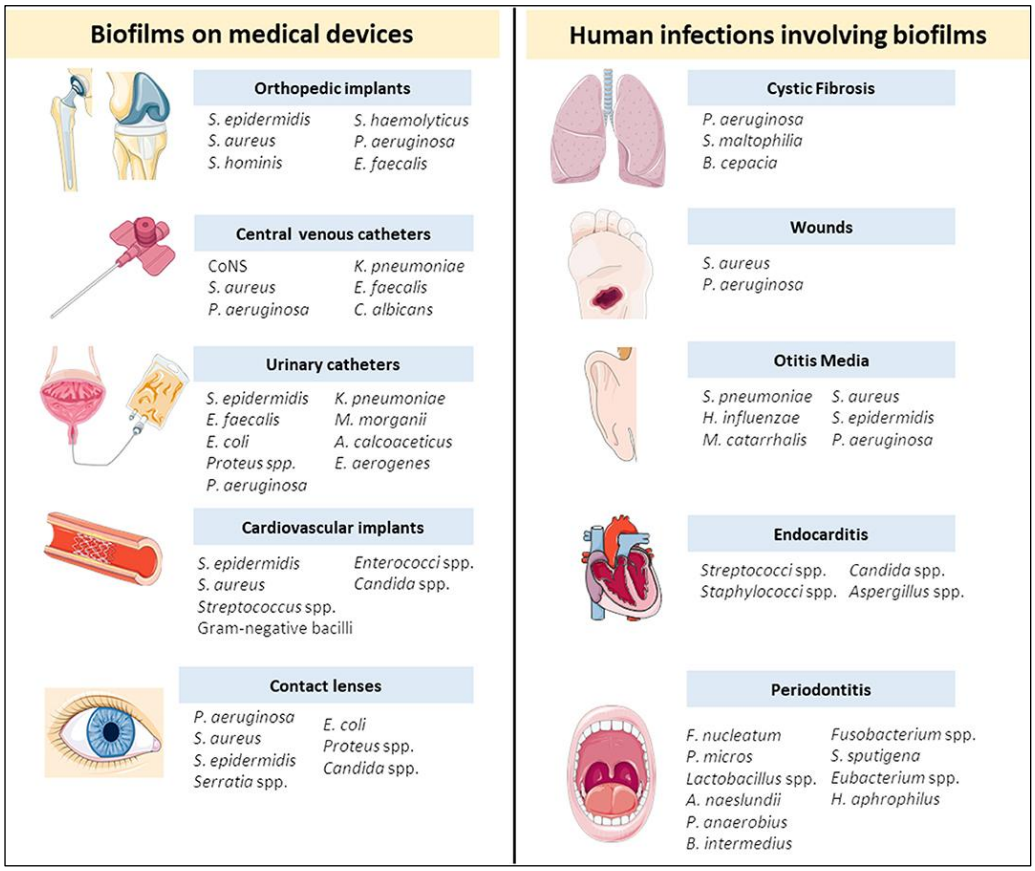

Figure 2. Schematic overview of common clinical contexts in which biofilms are formed, including biofilms on medical devices and biofilm-driven human infections. Representative bacterial and fungal species frequently associated with each condition are shown. Adapted from (Pinto et al., 2020)

Staphylococcus aureus is a key pathogen in this context and is one of the most widespread bacterial pathogens associated with clinical infection (Cheung et al., 2021). It is a primary causative

agent of numerous device- and procedure-associated infections, including bacteraemia, sepsis, catheter-associated bloodstream infections, ventilator-associated pneumonia, surgical site infections, and infections involving prosthetic materials and other implanted devices (Cheung et al., 2021; Tong et al., 2015). Its clinical significance is further increased by its capacity for antimicrobial resistance and robust biofilm formation (Cheung et al., 2021; Otto, 2018). In particular, methicillin-resistant *S. aureus* (MRSA) has been identified as a leading cause of antimicrobial resistance-related deaths (Samia et al., 2022). Currently, MRSA accounts for ten times as many infections as all multidrug-resistant (MDR) gram-negative pathogens (Craft et al., 2019). Furthermore, recent findings indicate that biofilm formation is strongly associated with multi-drug resistance in *S. aureus* infections (González-Vázquez et al., 2024). From a clinical perspective, surface samples suggest that biofilm formation serves as a reliable indicator of antibiotic-tolerant *S. aureus* populations, supporting chronic infection and environmental survival (Odoyo et al., 2023). The combination of antibiotic resistance and biofilm-related durability allows *S. aureus* to survive treatment and persist in healthcare settings.

These features make biofilms a critical healthcare problem, as they are widespread, persistent, resistant to antimicrobial treatment and disinfection, and can drive recurrent infection from devices and surfaces. *S. aureus* is a significant biofilm-forming pathogen because of its prevalence, clinical severity, resistance, and ability to colonise sites such as catheters, implants, and intensive care equipment. These insights highlight the need for effective surface-based strategies to reduce biofouling and infection risks in healthcare.

1.2. Current antibiofilm surface strategies and their limitations

1.2.1. Conventional strategies: Disinfectants

Chemical disinfection is a routine component of hospital infection control and is applied to surfaces, instruments, and the skin (Exner et al., 2020). The main classes of disinfectants, including oxidising agents, alkylating agents, alcohols, and membrane-active compounds, act by damaging microbial cell membranes, proteins, or nucleic acids (Maillard & Pascoe, 2024). However, their effectiveness in real clinical settings depends strongly on factors, such as contact time, organic load, surface type, and application frequency (Otter et al., 2015). Traditional infection control models focus on planktonic bacteria and short exposure testing. However, hospital contamination often involves biofilms that are structurally protected and more tolerant to antimicrobials (Maillard & Centeleghe, 2023). Several studies have shown that disinfectants are generally less effective against biofilm-associated bacteria than against planktonic cells (Naves et al., 2010; Todorić et al., 2023). This reduced susceptibility is mainly related to restricted disinfectant penetration, protection by the extracellular matrix, slow-growing or dormant cells, and stress-response mechanisms within the biofilm (Pallós et al., 2024). In addition, sublethal exposure could promote stronger biofilm formation and increased

antibiotic resistance (Maillard & Pascoe, 2024). Therefore, the use of disinfectants alone may not reliably ensure effective protection of surfaces against biofilm growth in clinical environments. In turn, the suboptimal use of disinfectants to treat biofilms may result in the spread of more tolerant and persistent biofilm communities and phenotypes. Because treatment of established biofilms is structurally disadvantaged, increasing attention has shifted toward preventative surface strategies designed to interfere with attachment and early colonisation before mature biofilms develop.

1.2.2. Preventive surface modification approaches

Surface modification strategies reduce microbial colonisation by altering material chemistry or structure to prevent adhesion, release antimicrobial agents, kill cells on contact, or activate antimicrobial effects in response to stimuli (Mu et al., 2023). In this review, these approaches are discussed according to their mechanism of action and summarised in Figure 3.

Anti-adhesive surfaces

Anti-adhesive surfaces target the earliest stage of biofilm formation by making attachment energetically or physically less favourable. These strategies operate through steric and electrostatic repulsion or reduced surface energy, which together limit initial microbial contact with the surface (Uneputty et al., 2022).

Polymer brush coatings, such as polyethylene glycol (PEG) and zwitterionic materials, have been widely studied. PEG forms a hydrated layer that reduces protein adsorption and microbial adhesion (Gon et al., 2012). However, PEG is susceptible to oxidative degradation and shows limited stability under biological conditions, thus constraining long-term performance (P. Zhang et al., 2016). In contrast, zwitterionic polymers, which retain large amounts of water through strong electrostatic interactions, generally show improved resistance to oxidants and sterilisation procedures (Moayedi et al., 2024). However, their synthesis is more complex, their mechanical robustness can be limited, and their sustained antifouling performance under routine use conditions remains uncertain (Amoako et al., 2025). Both systems rely on maintaining a dense, continuously hydrated polymer layer, which is difficult to preserve on frequently handled and cleaned clinical surfaces. Abrasion, drying, and exposure to cleaning agents can rapidly disrupt these coatings, compromising their protective function (S. Liu et al., 2022).

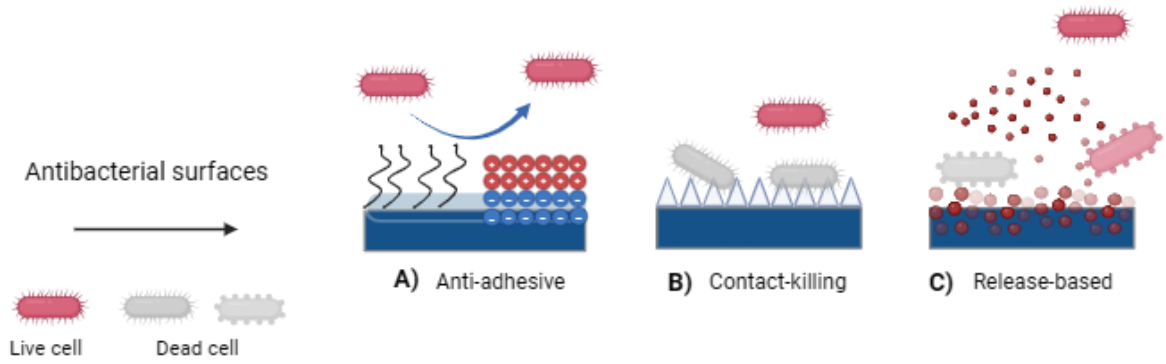

Figure 3. Schematic representation of classical antibacterial surface strategies: (A) anti-adhesive surfaces that prevent bacterial attachment, (B) contact-killing surfaces that inactivate bacteria upon direct contact, and (C) release-based surfaces that deliver antimicrobial agents to the surrounding environment. Red cells indicate viable bacteria; grey cells indicate dead bacteria

Release-based antibacterial surfaces

Release-based antibacterial surfaces embed antimicrobial agents into a coating and gradually release them into the surrounding environment (Uneputty et al., 2022). Depending on the system, these agents may include antibiotics, metal ions, antimicrobial peptides, nitric oxide donors, gas transmitters, and other bioactive compounds (Cloutier et al., 2015). The released agents disrupt the membranes, metabolism, or DNA of organisms, such as *S. aureus* and *E. coli* (Tomić & Vuković, 2022). However, their main limitation is that the antimicrobial effect is finite. Activity decreases as the reservoir is depleted, and surface fouling may further restrict the release (Pereira-Silva et al., 2025). In addition, mature and polymicrobial biofilms frequently show tolerance to released agents, reducing their long-term effectiveness (Nnaji et al., 2024). In contrast to stimuli-responsive systems, which can be repeatedly reactivated without consuming the active component, release-based approaches depend on continuous material depletion, making them less suitable for long-term surface applications.

Contact-killing antimicrobial surfaces

Contact-killing surfaces are designed to kill microorganisms upon direct contact without releasing antimicrobial agents into the surrounding environment (Kaur & Liu, 2016). Cationic surfaces are the most widely studied examples and typically act through electrostatic interactions with negatively charged microbial membranes, leading to membrane disruption and cell death. These surfaces are functionalized with positively charged chemical groups or molecules, such as amines, guanidinium, phosphonium salts, quaternary ammonium compounds, and polycations (Yang et al., 2018). Among these, quaternary ammonium compounds are among the best established (Santoro & Izzo, 2024). Although contact-killing strategies avoid the depletion problem associated with release-based coatings, their activity depends on the continuous accessibility of the active surface groups. In practice,

these groups may become masked by proteins, organic matter, dead cells, or other surface contaminants, resulting in reduced antimicrobial performance (Wilkinson et al., 2025).

Stimuli-responsive surfaces

Stimuli-responsive antimicrobial surfaces become active only after exposure to a specific trigger, such as light, temperature, pH, enzymes, or redox conditions (Guo et al., 2025; T. Zhang et al., 2024). This distinguishes them from static coatings, the antimicrobial function of which is continuously present and may decrease as the active agents are depleted or the surface groups are masked.

Light-responsive systems are particularly relevant for antimicrobial surface applications because their activity can be externally controlled in space and time. In these materials, illumination can activate photodynamic reactions, photothermal effects, or light-triggered release mechanisms (X. Wang, Shan, et al., 2022). Among them, photodynamic systems are particularly attractive because light activation of an incorporated photosensitizer generates reactive oxygen species (ROS), which can damage multiple microbial targets and reduce reliance on single-target antimicrobial mechanisms (X. Li et al., 2017). This makes antimicrobial photodynamic therapy (aPDT) a relevant approach for developing non-leaching, light-activated antimicrobial surfaces.

1.3. Antimicrobial photodynamic therapy (aPDT)

Antimicrobial photodynamic therapy (aPDT) uses light, a photosensitizer (PS), and oxygen to generate reactive oxygen species (ROS) that damage microbial cells. For surface applications, aPDT is attractive because antimicrobial activity is produced locally and only upon illumination, enabling spatial and temporal control without the continuous release of active agents.

1.3.1. Principles of aPDT and the basis of ROS-mediated killing

aPDT employs visible light of a specific wavelength to excite the PS in the presence of oxygen (Hamblin, 2016). Upon illumination, the photosensitizer transitions from its lowest energy level (ground-state singlet ^{1}PS) to an excited singlet state (^{1}PS*) and then to a longer-lived excited triplet state (^{3}PS*). From here, it can react with the surrounding molecules via two major pathways. The Type I mechanism involves electron or hydrogen transfer from one molecule to another to produce toxic reactive oxygen species, such as superoxide ($O_2\bullet^-$) and hydroxyl (•OH) radicals. In Type II reactions, the PS transfers its energy directly to molecular oxygen, producing singlet oxygen ($^1O_2$) with oxidising properties (Klausen et al., 2020). These two reactions can occur simultaneously and are dependent on factors, such as oxygen availability, PS structure, pH, and the surrounding microenvironment (Kwiatkowski et al., 2018). These processes occur within microseconds, and the resulting oxidants damage lipids, proteins, nucleic acids, and membrane systems (Hamblin, 2016). Figure 4 illustrates these photophysical transitions and the Type I and Type II ROS generation pathways that

underlie aPDT. The breadth of potential damage is central to aPDT's antimicrobial performance, which does not rely on the inhibition of a single biochemical pathway but instead produces oxidative stress across several essential cellular components simultaneously (Klausen et al., 2020).

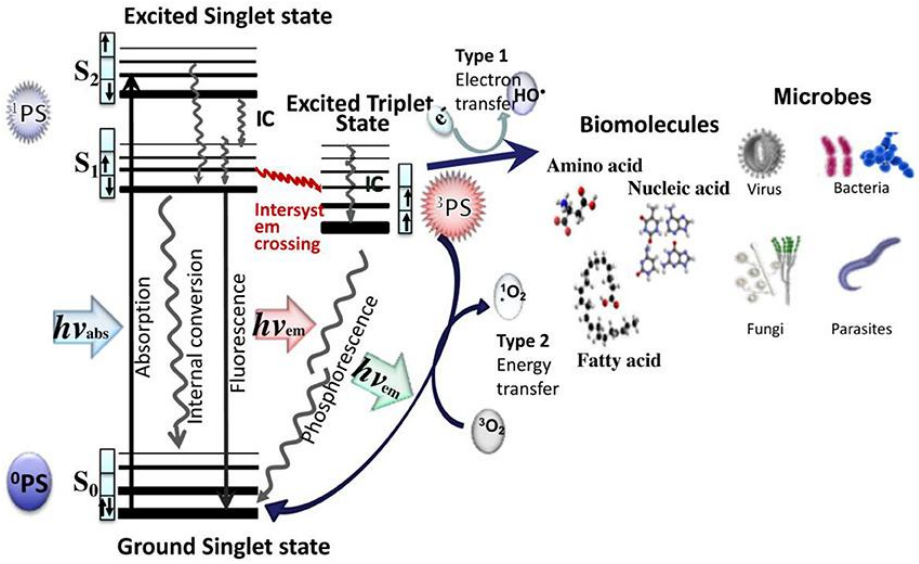

Figure 4. Jablonski diagram illustrating the Type I and Type II ROS generation mechanisms central to aPDT. Adapted from (Hu et al., 2018)

Because ROS damages multiple cellular targets, aPDT is generally associated with a lower risk of resistance development than single-target antimicrobials (Rapacka-Zdończyk et al., 2021). Some studies have used aPDT in combination with conventional antibiotics to increase MRSA susceptibility (Gonçalves et al., 2024). However, repeated sublethal exposure can promote tolerance, making uniform photosensitizer distribution and sufficient light penetration important design parameters for surface-based systems (Rapacka-Zdonczyk et al., 2021).

1.3.2. Effectiveness of aPDT against biofilm formation

aPDT can act at several stages of microbial-mediated surface colonisation. Photoactivated surfaces may inactivate planktonic cells during initial contact and damage newly attached cells before a mature biofilm develops. Before stable attachment, planktonic microorganisms encountering a photoactivated surface experience a localised burst of oxidative stress. A schematic representation of the antimicrobial mechanisms of ROS against biofilms and microbial cells is shown in Figure 5.

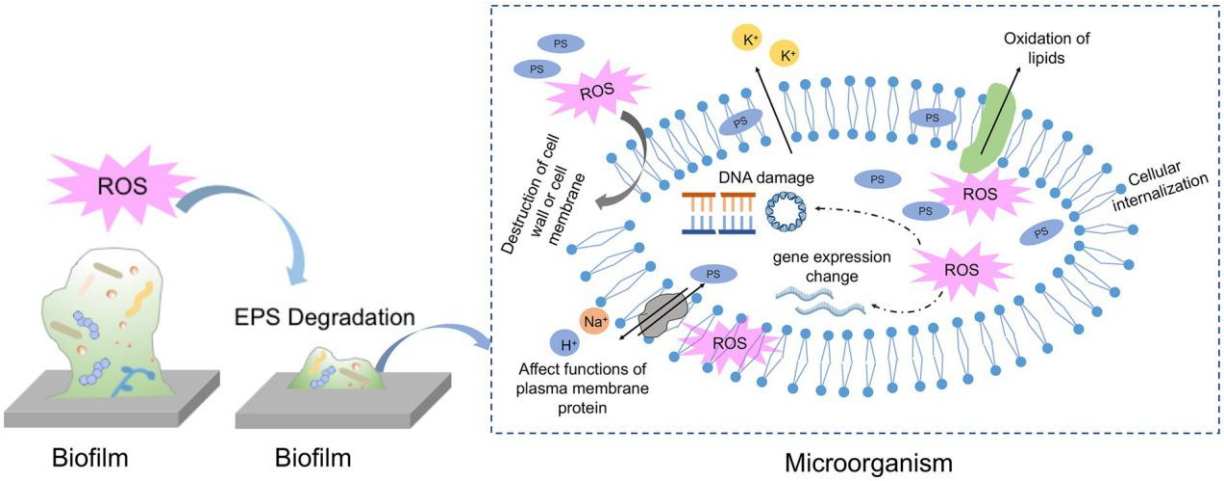

Figure 5. Schematic illustration of reactive oxygen species (ROS)-mediated antimicrobial mechanisms during antimicrobial photodynamic therapy (aPDT) against mature biofilms and individual microbial cells. Adapted from (Y. Li et al., 2023)

ROS-induced biocidal effects can reduce cell viability and limit the number of organisms available to initiate colonisation. Surface-based aPDT has consistently demonstrated antimicrobial activity against planktonic populations in experimental settings (Lavaee et al., 2022; Luke-Marshall et al., 2020; Reynoso et al., 2019).

1.3.3. Photosensitizers

Photosensitizers are light-responsive components of aPDT, and their behaviour under illumination determines the effectiveness of ROS generation at the material-microbe interface. The molecular properties of individual photosensitizers dictate whether these processes can be reliably sustained in practical antimicrobial settings (Klausen et al., 2020).

Photosensitizers used in aPDT can be broadly classified according to their chemical structure, which also predicts many of their functional properties (Escudero et al., 2021). Three major structural groups are commonly distinguished in the literature: **(i)** tetrapyrrolic macrocycles, such as porphyrins, chlorins, and phthalocyanines, which have been extensively used in both antimicrobial and clinical photodynamic applications (Bunin et al., 2023); **(ii)** organic dyes, including phenothiazinium, xanthene, and cyanine derivatives, which offer strong visible-light absorption but often lack long-term photostability (Moneira et al., 2012); and **(iii)** nanomaterial-based photosensitizers, in which the light-absorbing unit is a nanoscale scaffold rather than a classical dye (X. Wang, Zhu, et al., 2022). Fullerenes (C_{60} and related derivatives) fall within this third group and represent one of the best-characterized carbon-based systems capable of mediating ROS formation (Hamblin, 2018).

Because immobilised photosensitizers must function without replenishment or redistribution, their operational requirements change. Surface-bound molecules cannot diffuse freely and are not

replenished during treatment. Therefore, their performance depends strongly on their photostability, aggregation behaviour, and compatibility with the host material (Dube, 2024). Immobilised photosensitizers must remain chemically intact during storage and use, resist photobleaching under repeated illumination, and avoid aggregation within the coating or matrix, as aggregation can drastically shorten excited-state lifetimes and reduce reactive oxygen species (ROS) yields (Spagnul et al., 2015). Structural features, such as overall charge, hydrophobicity, and rigidity, play a crucial role in the association of photosensitizers with microbial cells, their dispersion in polymeric or inorganic matrices, and the preservation of their photochemical activity when confined to a surface (Pucelik et al., 2024). Fullerenes, known for their high triplet yield, function through both Type I and II pathways and resist photobleaching. However, their hydrophobic nature necessitates chemical modification for use in aqueous environments (Hamblin, 2018). These characteristics make them ideal for antimicrobial surfaces, where immobilised photosensitizers must remain active over numerous light cycles, thus justifying a focus on C_{60}-based systems in the next section.

1.3.4. Fullerene-Based Photosensitizers

Photophysical properties of C_{60} relevant to aPDT

Fullerenes form a distinctive family of all-carbon nanomaterials, with buckminsterfullerene (C_{60}) being the most widely studied. Structurally, C_{60} comprises a rigid spherical cage composed of fused aromatic rings arranged in a highly symmetric fashion (Figure 6). This architecture creates an extended π-conjugated system that allows C_{60} to absorb UV and visible light efficiently and facilitates the rapid population of a long-lived triplet state after photoexcitation (Pan et al., 2020). Unlike many organic dyes, C_{60} is exceptionally resistant to photodegradation, allowing repeated illumination cycles without loss of activity. Long-lived triplet states and photostability are major advantages of fullerenes for repeated use in surface coatings, where photosensitizers cannot be replenished or redistributed (Hamblin, 2018).

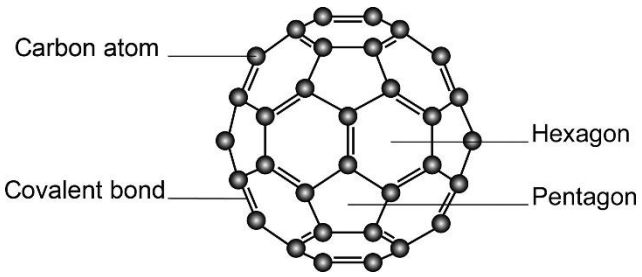

Figure 6. Structure of C_{60} fullerene (Buckminsterfullerene). Adapted from (Rondags et al., 2017)

Once excited to the triplet state, C_{60} can generate ROS via both Type I and Type II mechanisms. As a strong electron acceptor, it readily participates in electron-transfer reactions that give rise to

radical species, such as superoxide, hydrogen peroxide, and hydroxyl radicals; in contrast, energy transfer from the triplet state to molecular oxygen produces singlet oxygen. The balance between these pathways depends on the surrounding microenvironment. C_{60} often produces more Type I radicals under polar or reducing conditions, which may be advantageous on hospital surfaces, where oxygen concentration and hydration levels vary (Quinones et al., 2014). The ability to operate efficiently through both mechanisms expands the functional range of fullerenes compared to photosensitizers that rely on either singlet-oxygen production or radical pathways.

Safety and selectivity in clinical environments

Fullerenes exhibit advantageous safety profiles when employed as surface-bound photosensitizers in clinical settings. Pristine C_{60} displays very low dark toxicity, an important feature for hospital surfaces that are frequently touched but not continuously illuminated (Back et al., 2007). In addition, fullerene-based systems demonstrate selective microbial killing with low phototoxicity toward mammalian cells under selected experimental conditions (Bolshakova et al., 2023), a property attributed to differences in cell wall structure and ROS susceptibility. However, dose, composition, and exposure time can affect the toxicity of fullerene-based compounds, whereas incorporation into composite systems, for example, polymer carriers, can stabilise the dispersion and improve biological compatibility (Bolshakova et al., 2023).

Overcoming C_{60} limitations for surface-based aPDT

The main limitation of pristine C_{60} is its hydrophobicity, which promotes aggregation in aqueous environments and reduces ROS production by shortening the excited-state lifetimes (Lee et al., 2008). To overcome this limitation, extensive studies have focused on the functionalization of C_{60} to introduce hydrophilic, cationic, or amphiphilic groups that improve dispersion and enhance microbial association. An alternative approach, which is highly relevant to surface-based systems and the present work, relies on incorporating unmodified C_{60} into polymer matrices rather than in solution. Polymers can separate individual fullerene molecules, prevent aggregation, and maintain access to oxygen without altering the photophysical properties of C_{60} (Hou et al., 2022). Several studies have shown that polymer-supported C_{60} retains strong photodynamic activity: polymer nanoparticles containing unmodified C_{60} generate ROS efficiently under illumination and exhibit photodynamic effects in biological assays (D. Wang et al., 2023); polymer films embedding C_{60} units can photoinactivate *S. aureus* upon irradiation (Ballatore et al., 2015); and polymer-stabilized C_{60} dispersions maintain fullerene reactivity in aqueous environments by preventing aggregation (Samoilova et al., 2024). This evidence suggests that a combination of C_{60} and a polymer carrier is a viable and effective strategy for using pristine C_{60} in photodynamic applications. Therefore, this work will focus on the incorpo-

ration of pristine C_{60} into biocompatible polymer matrices using a thermomechanical processing approach to produce solid composite films for antimicrobial surface applications. The following section highlights the evidence supporting this experimental approach.

1.3.5. Polymer–fullerene systems for antimicrobial coatings

Polymer–fullerene films provide several advantages over solution-based or nanoparticle fullerene formulations when used as antimicrobial coatings. Embedding C_{60} within a solid polymer matrix physically immobilises the photosensitizer, preventing leaching or particle migration during use and cleaning, while ensuring stable and reproducible photoactivity upon illumination (Gonzalez et al., 2023; Reynoso et al., 2021). A solid film also provides a mechanically robust framework capable of withstanding abrasion and routine disinfection, both critical for maintaining performance on high-contact clinical or public surfaces (Savagatrup et al., 2014). Moreover, immobilisation allows for a defined spatial distribution of the fullerene, producing predictable reactive oxygen species (ROS) generation under light exposure, unlike dispersive systems that may suffer from aggregation, sedimentation, or aging effects (Prylutskyy et al., 2013). A study conducted by Alekseeva et al. (2017) on the structural properties and biological activity of polystyrene-fullerene composite films is a good example of such systems. The authors reported that antibacterial activity against E. coli and S. aureus increased after fullerene incorporation (Alekseeva et al., 2018). However, this effect was not light-activated and was attributed mainly to interactions between fullerenes and microbial cell components.

The choice of polymer matrix is as important as that of the photosensitizer. Polymers, such as polylactic acid (PLA), poly(3-hydroxybutyrate-co-3-hydroxyvalerate) (PHBV), and chitosan, offer a combination of biocompatibility, optical transparency in the visible range, and mechanical durability, making them suitable for antimicrobial photodynamic therapy (aPDT) applications. PLA and PHBV are widely used in biomedical and food-contact materials owing to their recognised safety and processability (Hussain et al., 2024; Ibrahim et al., 2021; Moll & Chiralt, 2026; Z. Naser et al., 2021), whereas chitosan contributes additional intrinsic antimicrobial effects and biodegradability (Dash et al., 2011; Yadav et al., 2024). These biopolymers have been approved for indirect and direct biological contact, emphasising their translatability for antimicrobial coatings in clinical or environmental settings (Y. Liu et al., 2021; Navarro et al., 2004; Sultana Phd Ceng Csci & Wang, 2011).

1.3.6. Thermomechanical Processing of Polymer–Fullerene Composites

Despite the promise of polymer-fullerene photodynamic systems, their fabrication methods primarily rely on chemical synthesis and solution casting. These techniques can produce uniform lab-scale films. However, they often involve hazardous solvents, complex chemistry, and limited scalability. (Fawaz & Mittal, 2014; Tran et al., 2025). In contrast, thermomechanical processing methods, including extrusion, compression moulding, and injection moulding - represent mature industrial

technologies capable of producing durable polymer composites at scale with high reproducibility and solvent-free operation (Botta et al., 2014; El Moumen et al., 2019).

Melt processing allows for the solvent-free integration of photoactive fullerenes into thermoplastic matrices, ensuring the stable immobilisation and mechanical integrity of the photosensitizer (Wylie et al., 2021). Previous studies have demonstrated the successful dispersion of fullerene C_{60} into thermoplastics for electronic, mechanical reinforcement, and thermal stability applications, confirming its compatibility with melt-based techniques (Penkova et al., 2017; Pereira et al., 2015). However, the use of these methods to create photoactive antimicrobial films remains unexplored. The few existing reports on photodynamic antimicrobial coatings, such as PEDOT–C_{60} electropolymeric films (Reynoso et al., 2019) or fullerene-modified PLA composites (Saulėnienė et al., 2024), underscore the potential of fullerenes as stable and light-responsive additives. However, they rely on electrochemical or solution-based synthesis approaches rather than scalable industrial processing.

The present work addresses this methodological gap by applying conventional thermomechanical polymer processing techniques to fabricate polymer–fullerene films designed for antimicrobial photodynamic surface applications. The suitability of biopolymers for thermomechanical processing depends strongly on their chemical structure (Figure 7). PLA and PHBV are thermoplastic aliphatic polyesters that can therefore be processed using conventional melt-based methods. In contrast, chitosan is a polysaccharide containing hydroxyl and amino groups, with strong intermolecular interactions and limited melt processability under conventional conditions. These structural differences are important for understanding why different fabrication routes were required in the present work.

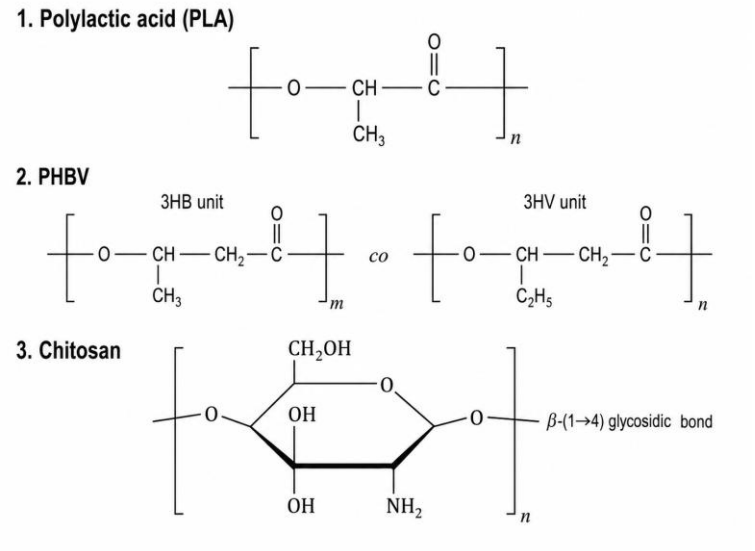

Figure 7. Representative structural fragments of the biopolymers used in this work: poly (lactic acid) (PLA), poly(3-hydroxybutyrate-co-3-hydroxyvalerate) (PHBV), and chitosan. PHBV is shown as a copolymer composed of 3-hydroxybutyrate (3HB) and 3-hydroxyvalerate (3HV) repeating units

Thus, although all three materials were selected as biopolymer matrices for C_{60} incorporation, their structural differences required adaptation of the processing strategy. This consideration underlies the experimental design used in the present study.

2. Materials and Methods

2.1. Film fabrication

Neat and fullerene-incorporated biopolymer films were fabricated at the Research Center for Naval and Industrial Technologies (CITENI), University of A Coruña, Spain, during a research internship. A thermomechanical processing approach was employed to produce biopolymer films. Three polymer systems were investigated: poly(lactic acid) (PLA; PLA-Premium pellets, AD Bioplastics, Paterna, Valencia, Spain), poly(3-hydroxybutyrate-co-3-hydroxyvalerate) (PHBV; 12 wt % hydroxyvalerate (3HV), Mw ≈ 240,000, plasticized with 10 wt% citric acid, Goodfellow Ltd., Cambridge, UK), and chitosan (low molecular weight, viscosity 30–100 cps, Mw ≈ 250,000 g·mol^{-1}, CAS: 9012-76-4, Glentham Life Sciences Ltd., Corsham, UK). From each polymer, neat and composite films containing 0.5 wt% fullerene-C_{60} (≥98% purity, Sigma-Aldrich; CAS: 99685-96-8) were prepared. Due to differences in thermal processability, two fabrication routes were used. Thermoplastic polymers (PLA and PHBV) were processed through a three-step processing route involving extrusion, injection moulding, and hot pressing. In contrast, chitosan films were produced by hot pressing only.

2.1.1. Thermoplastic polymer film (PLA and PHBV) fabrication

Prior to processing, PLA and PHBV pellets were dried at 70 °C for 24 h to remove residual moisture. Extrusion was carried out using a twin-screw extruder (Haake Force Feeder Minilab II, UK) equipped with conical counter-rotating screws and an integrated backflow channel. The extrusion parameters for both polymer systems are listed in Table 1.

Table 1. Extrusion parameters used for PLA and PHBV processing

Polymer	Temperature	Screw speed	Processing time
PLA	170 °C	100 rpm	5 min
PHBV	165 °C	60 rpm	5 min

Following extrusion, the materials were injection moulded into uniform circular samples using a mini-injection moulding device (Thermo Fisher Scientific HAAKE MiniJet II, Karlsruhe, Germany). The injection parameters are summarized in Table 2.

Table 2. Injection moulding parameters

Polymer	Cylinder temperature	Mold temperature	Injection conditions
PLA	165 °C	60 °C	6 s at 800 bar + 3 s at 500 bars
PHBV	160 °C	50 °C	6 s at 800 bar + 3 s at 500 bars

Finally, films of approximately 0.2 mm were produced by a heating press IQAP-LAB PL-15 (IQAP Masterbatch Group S.L., Barcelona, Spain). The processing parameters used for film formation are presented in Table 3. Neat PLA and PHBV films were processed under identical conditions with their composite films to enable direct comparison.

2.1.2. Chitosan film fabrication

To prepare neat and composite films, chitosan powder was first premixed with C_{60} powder (0.5% wt). Glycerol (vegetable glycerine, cosmetic/technical grade, Plantawa, Spain) was added to chitosan or chitosan-C_{60} powder mix dropwise until a homogeneous paste was obtained, maintaining a chitosan: glycerol ratio of 2:1 (w/w). In the following step, 3% (v/v) aqueous acetic acid solution was gradually added to the samples under manual mixing to obtain a uniform dispersion. The chitosan: acetic acid aqueous solution ratio was maintained at 25:75 (w/w). The mixture was manually mixed for 15 min to obtain a homogeneous material. Chitosan films were produced by hot pressing (processing parameters presented in Table 3). The prepared formulation was placed into circular cavities of a metal mould plate with a diameter of 1 cm and a thickness of 0.2 cm (2 mm). The mould was then subjected to hot pressing to form films with uniform geometry. After pressing, the mould was allowed to cool before the solidified films were removed.

Table 3. Hot pressing parameters used for the fabrication of PLA, PHBV, and chitosan films

Polymer	Temperature	Pressure	Time
PLA	165 °C	20 bars	5 min
PHBV	160 °C	10 bars	3 min
Chitosan	105 °C	40 bars	7 min

2.2. Physical and Chemical Characterization of Films

2.2.1. Raman spectrophotometry

The Raman spectra were acquired at the Center for Physical Sciences and Technology, Department of Organic Chemistry in collaboration with Dr. Martynas Talaikis using Raman microscope (Renishaw, UK) equipped with a thermoelectrically cooled CCD detector (−70 °C). Excitation was provided by a 785 nm laser, and spectra were recorded using a 1200 lines/mm grating. The laser power was set to 50 mW, and the beam was shaped into a line focus of approximately 50 µm × 10 µm on the sample using a 20×/0.40 NA objective lens. Hyperspectral maps were acquired with 1 s integration per spectrum using a spatial step size of 13.5 × 20.0 µm. Each map comprised approximately 500 spectra collected on a 33 × 15 grid. The Raman wavenumber axis was calibrated using the silicon standard peak at 520.7 cm^{-1}.

2.2.2. X-ray diffraction

XRD patterns of studied raw polymer material, neat polymer films and composite films were measured at the Center for Physical Sciences and Technology, Department of Characterisation of Materials Structure in collaboration with Dr. Vidas Pakštas. Measurements were performed using an X-ray diffractometer Smart Lab (Rigaku) equipped with an X-ray tube with a 9-kW rotating Cu anode. Furthermore, Bragg–Brentano geometry with a graphite monochromator on the diffracted beam and a step scan mode with a step size of 0.02° (in 2θ scale) and counting time of 1s per step was applied. The measurements were conducted in the 2θ range of 5–75°. Phase identification was performed using the software package PDXL (Rigaku) and the ICDD powder diffraction database PDF4+ (2024 release). The size of the crystallites was calculated based on the broadening of XRD peaks using the graphical Halder–Wagner method implemented into PDXL software.

2.2.3. Differential Scanning Calorimetry (DSC)

The thermal behaviour of studied raw polymer material and composite films was analysed at the Research Center for Naval and Industrial Technologies (CITENI), University of A Coruña, Spain, in collaboration with Dr. María Belén Montero Rodríguez. Measurements were performed using a PerkinElmer Pyris Diamond DSC 7 differential scanning calorimeter (PerkinElmer Spain SL, Madrid, Spain) operating under the power compensation principle. Experiments were conducted under a nitrogen atmosphere with a flow rate of 80 mL min^{-1}, using liquid nitrogen–controlled cooling. Samples were sealed in aluminium pans prior to analysis.

A heat–cool–heat thermal program was applied. The temperature ranges were selected according to the polymer system:

1) PLA: 30–240 °C

2) PHBV: 30–210 °C
3) Chitosan: 30–250 °C

Samples were cycled between 30 °C and the upper limit at 10 °C min⁻¹ in heat–cool–heat mode, with 1 min isothermal holds. The program concluded with a final cooling segment to 30 °C at 10 °C min⁻¹. Although both heating cycles were recorded, only the first heating scan was used for analysis and presentation of results, as it reflected the processing-induced thermal behaviour of the materials.

DSC raw heat-flow data were processed using OriginPro (2026), where the thermograms were plotted and thermal transitions were analysed. Peak temperatures were determined from the corresponding transition maxima or midpoints, depending on the type of transition. Enthalpy values were obtained by integrating the relevant peak areas after baseline correction. The enthalpy relaxation associated with the glass transition was reported as ΔH_relax. Cold crystallization enthalpy was reported as ΔHcc, while the exothermic event assigned to crystal reorganization/recrystallization was reported separately as ΔHreorg. Melting enthalpies were reported as ΔHm, and the total melting enthalpy, ΔHm, total, was calculated as the sum of all detected melting endotherms.

The degree of crystallinity, Xc, was calculated using:

$$X_c = \frac{\Delta H_{m,total} - \Delta H_{cc} - \Delta H_{reorg}}{\Delta H_m^0 \times w_{PLA}} \times 100$$

where $\Delta H_m^0 = 93$ J/g is the melting enthalpy of 100% crystalline PLA, and $w_{PLA}$is the PLA mass fraction in the analysed sample. For raw PLA, $w_{PLA} = 1$, while for PLA-C_{60} composite films, $w_{PLA}$was corrected according to the PLA content in the composite formulation.

2.3. Photochemical Analysis

Reactive oxygen species (ROS) generation by the C_{60}-containing films was evaluated using 9,10-dimethylanthracene (DPA, CAS: 1499-10-1, MW: 330.43 g·mol⁻¹; Fluorochem Ltd.) as a chemical probe for singlet oxygen. DPA reacts selectively with singlet oxygen to form an endoperoxide, resulting in a decrease in its characteristic absorbance band at 395 nm (Steinbeck et al., 1992), which was used to monitor ROS production. N, N-dimethylformamide (DMF, ACS Reagent grade) was used as the solvent for all measurements.

A calibration curve was established using DPA solutions in DMF over the concentration range of 0–185 μM. The optical density in the final volume did not exceed 1.5. The relationship between absorbance at 395 nm and DPA concentration was described by a linear equation (A = 0.0067C − 0.0022, R^2 = 0.9959), enabling conversion of absorbance values to DPA concentration.

For ROS measurements, DPA solutions with an initial concentration of 184.8 μM were prepared. Polymer films containing C_{60} were immersed in the DPA solution and irradiated with a blue LED source (450 nm, 10 mW; FTMC) for 2 h. The illuminated area corresponded to the sample diameter (0.5 cm), yielding a total light dose of approximately 367 J cm^{-2}, calculated as the product of light power and exposure time divided by the irradiated area. A control sample containing only DPA in DMF (184.8 μM) was irradiated under identical conditions to account for photobleaching of the probe.

After irradiation, the absorbance of each sample at 395 nm was recorded and converted to the corresponding DPA concentration using the calibration equation:

$$\text{ROS (mol)} = \textit{initial}\ \text{DPA (mol)} - \textit{measurement}\ \text{DPA (mol)}$$

To correct for photobleaching, the decrease observed in the control sample (6.7 μM) was subtracted. The ROS equivalents generated by each sample were calculated as the difference between the control-corrected DPA concentration and that of the irradiated sample.

All measurements were performed in replicate, and ROS values were calculated individually for each replicate prior to averaging. The assay volume was 4.2 mL. For comparative analysis, ROS production was further normalized either to the mass of the polymer film and to the mass of C_{60} present in each system, as described in the Results section.

2.4. Microbiological analysis

2.4.1. Preparation and Standardization of Bacterial Inoculum

To prepare the bacterial suspension used in subsequent assays (CFU enumeration, XTT assay and SEM analysis), 5 mL of Brain Heart Infusion broth (BHI, Biolab, Budapest, Hungary) was inoculated with 500 μL of *Staphylococcus aureus* (NCTC 11963) stock culture. The culture was incubated in a shaking incubator at 37 °C and 150 rpm for 18 h to obtain an overnight culture.

After incubation, the culture was centrifuged at 5000 rpm for 5 min, and the supernatant was discarded. The pellet was then resuspended in phosphate-buffered saline (PBS) and vortexed to obtain a uniform suspension, followed by centrifugation under the same conditions. This washing procedure—resuspension in PBS, vortexing, and centrifugation - was repeated two additional times, resulting in a total of three washing cycles to remove residual growth medium.

After the final wash, the pellet was resuspended in 5 mL of PBS and vortexed until a homogeneous suspension was obtained. The optical density (OD) of the suspension was measured at 600 nm using UV–Vis spectrophotometer (HALO RB-10, Dynamica GmbH, Salzburg, Austria).

The bacterial concentration was standardized to 10^7 cells/mL using the following equation:

$$V_0 = (Abs_0 \times V) / (5 \times Abs)$$

Where:

V_0 – volume of stock suspension required for dilution (mL);

Abs_0 – reference absorbance corresponding to a concentration of 10^7 cells/mL (0.427 for *S. aureus*);

V – final volume of the diluted suspension (mL);

5 – volume of the primary stock suspension (mL);

Abs – measured absorbance of the sample.

2.4.2. Colony-forming unit (CFU) assay

Colony-forming unit (CFU) assays were performed to evaluate whether light-activated C_{60}-containing films reduce the number of viable bacteria capable of persisting on the material surface. Therefore, the assay was designed to quantify recoverable surface-associated bacteria rather than the total bacterial population present in the well. Two experimental conditions were investigated: immediate surface-associated photoinactivation and photoinactivation of pre-attached cells. In each experiment, identical sets of samples were processed in parallel under light and dark conditions to serve as treated and control groups:

1) *Composite polymer-C_{60} film + light* as experimental treatment
2) *Composite polymer-C_{60} film + dark* as dark control
3) *Neat polymer film + dark* as baseline/negative control

Prior to assay, all samples were sterilized in 70% ethanol for 20 min and washed with PBS afterwards to remove the residual alcohol.

CFU assays were performed in three independent experiments on separate days. In each experiment, each condition was tested using three film discs, and suspensions containing recovered attached cells were plated in technical duplicate. Colony counts from technical duplicates were averaged before calculating $\log_{10}$ CFU/mL values.

Circular film samples (0.5 cm diameter) composed of biopolymer–fullerene composites and corresponding neat biopolymer controls without fullerene were placed into wells of sterile 24-well tissue culture plates. 1 mL *S. aureus* suspension was added to each well. For each assay, two plates were prepared simultaneously:

- one plate to be exposed to blue light
- one plate to be maintained in the dark as a control

Photoirradiation during bacterial attachment

To evaluate the effect of light-activated films during the initial contact between bacteria and the material surface, samples were immediately exposed to blue light for 2 h following the addition of the bacterial suspension. A second, dark control, plate containing samples was kept in the dark for the same duration at 37 °C.

After treatment, the samples were washed three times with PBS to remove non-adherent and weakly associated cells. The PBS wash fractions were discarded because this assay specifically aimed to quantify bacteria that remained associated with the film surface after treatment and washing. The remaining surface-associated cells were detached by transferring the samples into 2 mL microcentrifuge tubes containing 1 mL PBS and sterile 4 mm glass beads, followed by vortexing for 2 min. The resulting bacterial suspensions were serially diluted up to 10^{-3}, and 20 µL aliquots were spread onto brain heart infusion (BHI) agar plates. Plates were incubated overnight at 37°C, and the number of colonies was counted to determine the number of surviving bacteria.

This assay quantified the number of viable surface-associated bacteria remaining after immediate light exposure and washing.

Photoirradiation of pre-attached surface-associated cells

To evaluate the bactericidal activity against already attached bacterial populations, both treatment and control group samples were first incubated with bacterial suspension at 37 °C for 90 min in the dark to allow bacterial attachment. After this attachment period, the bacterial suspension was removed, and the samples were gently washed three times with PBS to eliminate non-adherent cells. The PBS wash fractions were discarded because the assay was focused on the bacterial population that remained attached to the film surface after the 90 min attachment period.

C_{60}-containing dark controls and corresponding neat polymer dark controls were processed immediately after the 90 min attachment period to determine the number of viable bacteria recoverable from the film surface. For the treatment group, fresh PBS was added to each well, and the samples were exposed to blue light for 2 h at room temperature. After irradiation, the samples were washed again with PBS to remove cells that were no longer firmly associated with the surface. Surface-associated cells remaining on the films were then recovered by vortexing the samples in PBS with sterile glass beads, followed by serial dilution and plating for CFU enumeration.

This assay therefore quantified the number of viable bacteria recoverable from the film surface after 90 min of attachment and compared it with the number remaining after subsequent blue-light treatment. The endpoint reflects photoinactivation and/or light-induced weakening of bacterial surface association, rather than total bacterial survival in the well.

2.4.3. XTT metabolic activity assay

The XTT metabolic activity assay was performed on the same recovered bacterial suspensions used for CFU enumeration. The assay was carried out for samples from both experimental set-ups after the corresponding light-exposed and dark control treatments. Following recovery of the attached bacterial cells from the film samples, an aliquot of each undiluted suspension was used directly for metabolic activity analysis.

For each sample, 100 µL of the recovered bacterial suspension was transferred into a well of a 96-well tissue culture plate. Blank wells and control wells were prepared in parallel. Neat polymer films kept in the dark were used as the 100% metabolic activity reference for each corresponding polymer system. C_{60}-containing films kept in the dark were used to evaluate the effect of fullerene incorporation without light activation, while illuminated C_{60}-containing films were used to evaluate the combined effect of fullerene incorporation and photoirradiation. The XTT labelling mixture from the Cell Proliferation Kit II (XTT; Roche) was prepared according to the manufacturer's instructions to a final XTT concentration of 0.3 mg/mL and added to the wells containing the bacterial suspensions. The plate was incubated at 37 °C for 24 h, after which absorbance was measured at 450 nm using a microplate reader. Absorbance values were used as an indicator of the metabolic activity of bacterial cells recovered from the film samples, with higher absorbance corresponding to greater metabolic activity.

Relative metabolic activity was calculated after blank correction using the following equation:

$$\text{Relative metabolic activity (\%)} = \frac{OD_{\text{sample}} - OD_{\text{blank}}}{OD_{\text{neat polymer dark}} - OD_{\text{blank}}} \times 100$$

For each polymer system, the corresponding neat polymer dark control was set as 100%. Values above 100% indicate that the recovered XTT signal was higher than that of the corresponding neat polymer dark control. Results were calculated from three independent experimental days and are presented as mean ± SD.

2.4.4. Scanning electron microscopy

SEM analysis was performed at the Faculty of Electronics, Vilnius Gediminas Technical University, with technical assistance from senior engineer Andrius Maneikis. Composite and neat film discs (0.5 cm diameter) of PHBV, PLA, and chitosan were sterilized in ethanol for 20 min and subsequently washed with phosphate-buffered saline (PBS) to remove residual ethanol. The films were placed in 24-well tissue culture plates and incubated with 1 mL of *Staphylococcus aureus* suspension (10^7 CFU/mL) for 90 min at 37 °C to allow bacterial attachment.

After incubation, the samples were washed three times with PBS to remove unattached cells. Subsequently, 1 mL of PBS was added to each well and the samples were exposed to blue light for 2 h. Following irradiation, PBS was removed and samples were thoroughly washed with PBS using vortex for 1 min, the procedure was repeated three times. The PBS from the last wash was replaced with 2.5% glutaraldehyde solution, and the samples were fixed for 2 h at 4 °C. The glutaraldehyde solution was then removed, and the samples were dehydrated through a graded ethanol series (30%, 50%, 70%, 90%, and 100%) for 10 min at each step. The samples were allowed to dry at room temperature in a laminar flow cabinet and stored at 4 °C until SEM analysis.

To mitigate surface charging and enhance secondary electron emission, all samples were coated with a tantalum (Ta) layer of 10–15 nm thickness. Metal layer was deposited using direct current magnetron sputter (manufacturer Vacuum System Technologies V.S.T. (SERVICES) LTD.) at room temperature using a 2-inch high-purity Ta target under an argon atmosphere at a working pressure of 15 mTorr. Surface morphology was subsequently characterized via scanning electron microscopy (SEM) using a Tescan Vega 3 system. Digital micrographs were acquired using a secondary electron (SE) detector to provide high-resolution topographical contrast.

3. Results

3.1. Fabrication of neat and C_{60}-containing biopolymer films

Neat and C_{60}-containing biopolymer films based on PLA, PHBV, and chitosan were successfully prepared under the optimized conditions described in the Materials and Methods section. Two fabrication routes were applied, depending on the processing behaviour of each polymer.

PLA and PHBV, which are thermoplastic polymers, were processed using a three-step thermomechanical route: extrusion, injection moulding, and hot pressing. In contrast, chitosan samples were produced by hot pressing in a mould plate after manual premixing with fullerene and plasticizers.

The multistep route produced uniform circular films of both neat and C_{60}-containing PLA and PHBV, with an approximate thickness of 0.2 mm. A general processing scheme and representative PLA and PHBV films are shown in Figure 8A. The neat films were light in colour and appeared macroscopically uniform. The corresponding composite films were darker and greyish, with fine visible speckling, indicating the presence of dispersed C_{60} within the polymer matrix (Figure 8 B,C).

For chitosan, the starting material was first manually premixed into a paste-like mass. This mixture was then placed into a metal mould and hot pressed to obtain smaller circular samples with an approximate thickness of 0.2 cm. Representative images of the premixed material, the mould, and the final chitosan sample are also shown in Figure 8D. These results show that film formation was

achieved for all three polymer systems, although the fabrication route depended on the type of polymer.

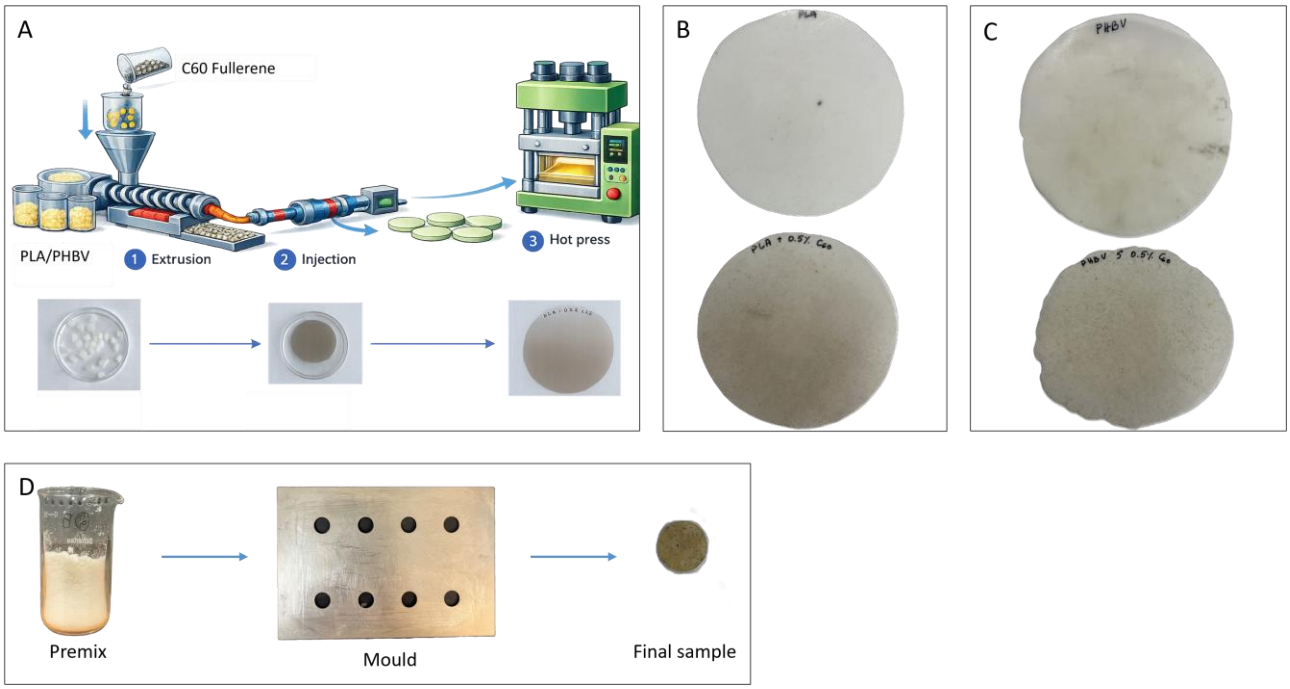

Figure 8. Fabrication routes and representative neat and C_{60}-containing biopolymer films. (A)Three-step thermomechanical processing route used for PLA and PHBV films, consisting of extrusion, injection moulding, and hot pressing. (B) Representative neat and 0.5 wt% C_{60}-containing PLA films. (C) Representative neat and 0.5 wt% C_{60}-containing PHBV films. (D) Chitosan fabrication route, showing premixed starting material, metal mould used for shaping, and representative hot-pressed chitosan sample

Overall, neat and composite samples were successfully obtained for all investigated biopolymer systems. The processing method, however, had to be adjusted according to the thermal and rheological properties of each polymer.

3.2. Structural confirmation of C_{60} incorporation in biopolymer films

3.2.1. Raman analysis of C_{60} incorporation and distribution in biopolymer films

The incorporation of fullerene into the polymer matrices was examined via Raman spectroscopy using 785 nm laser excitation. Figure 9A compares the Raman spectra of neat PLA, chitosan, and PHBV films with the films modified with fullerene. The modified samples exhibit distinct vibrational bands characteristic of fullerene. Most notably, all composite spectra exhibited the dominant Raman-active Ag (2) mode at approximately 1467 cm^{-1}. Additional fullerene markers are visible at 1575 (Hg (8)), 1249 (Hg (6)), and 772 cm^{-1} (Hg (4)), showing good agreement with the reference spectrum of pure fullerene (Figure 9B). The preservation of the Ag (2) mode position in the films

demonstrates that the fullerene structure was unaffected by either the polymer integration or the laser excitation.

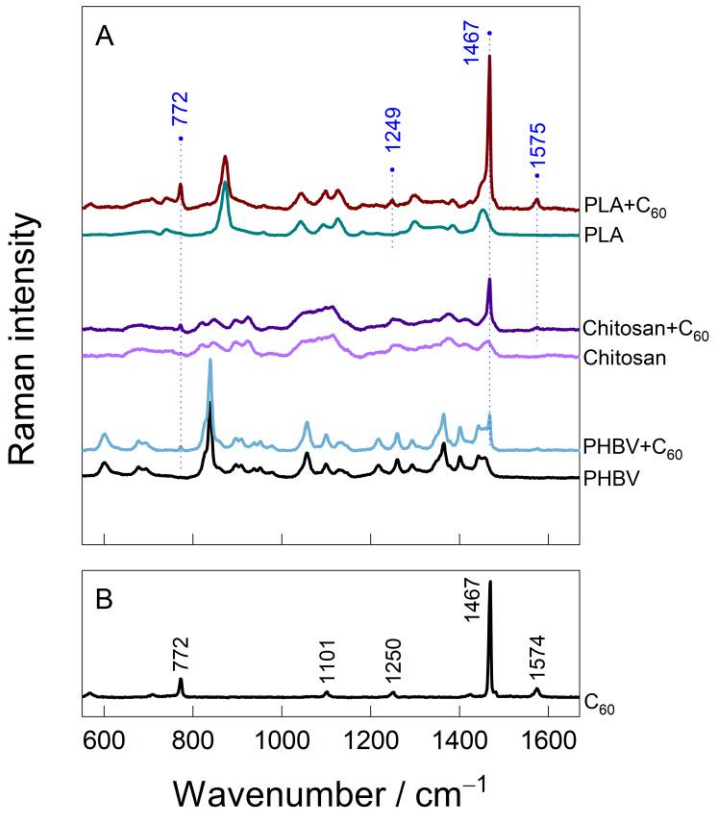

Figure 9. (A) Raman spectra of PLA, chitosan, and PHBV films with and without fullerene. Spectra were collected by averaging the Raman mapping data of ~500 individual spectra. (B) Raman spectrum of pristine fullerene C_{60}

Figure 10 displays the optical microscopy images alongside the corresponding Raman intensity maps, constructed by plotting the intensity at 1467 cm^{-1}. All polymer films exhibited a highly heterogeneous distribution of fullerene characterized by discrete regions of intense Raman scattering. Analysis of the mapping data indicates that the fullerene phase occupies approximately 10–15% of the scanned area. Moreover, the maximum intensity of Ag (2) mode recorded for PLA was 10500 counts, which is nearly an order of magnitude higher than that observed in the other matrices. This high signal intensity concentrated in specific domains suggests the formation of significant fullerene agglomerates or phase-segregated islands within the PLA matrix.

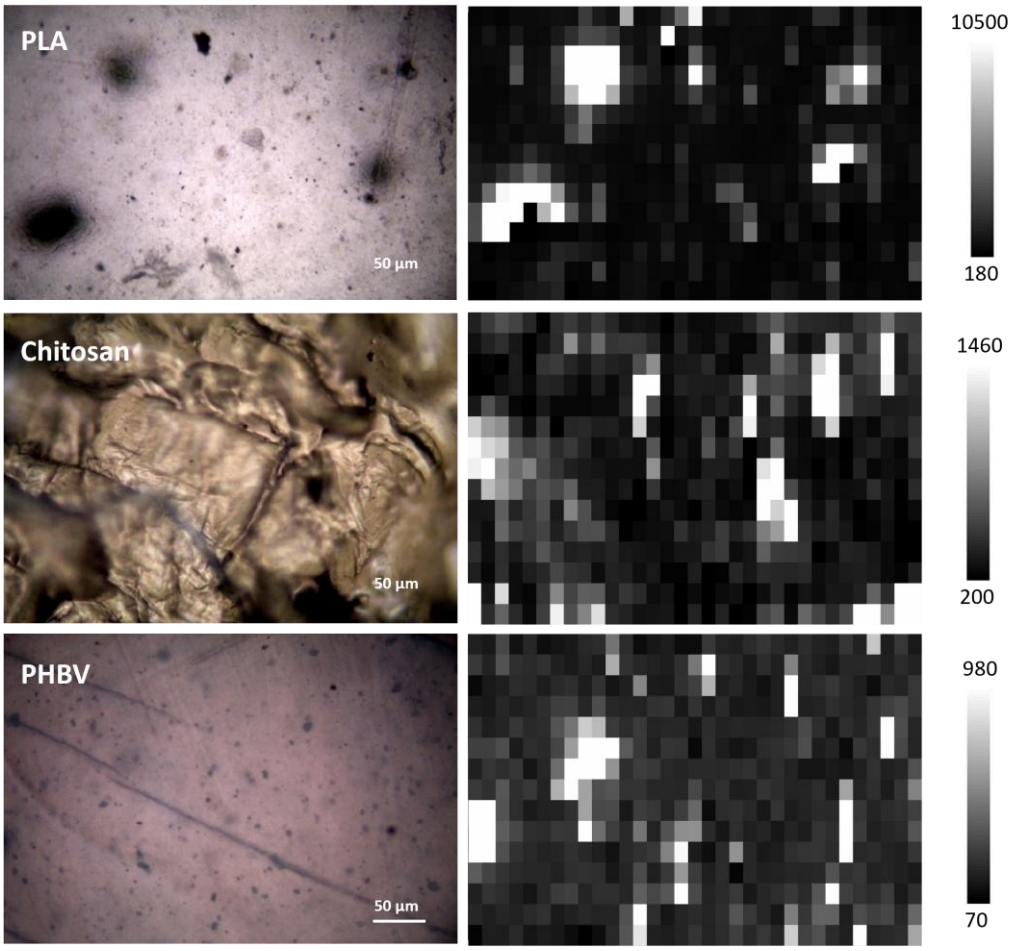

Figure 10. Optical microscopy images (left) and Raman intensity maps (right) based on the 1467 cm−1 band of fullerene incorporated into PLA, chitosan, and PHBV matrices. Raman maps were acquired with a spatial step size of 13.5 × 20.0 µm. The maximum intensity (white) corresponds to 10500 counts for PLA, 1450 counts for chitosan, and 1000 counts for PHBV

Overall, Raman spectroscopy confirmed the successful incorporation of C_{60} into all three biopolymer matrices, while Raman mapping showed that its distribution was heterogeneous and depended on the polymer system.

3.2.2. XRD analysis of crystalline structure and C_{60} reflections

XRD analysis was performed to evaluate the crystalline structure of the raw polymer materials, the thermally processed neat films, and the corresponding C_{60}-containing composite films of PLA, PHBV, and chitosan. The diffraction patterns of all systems are shown in Figure 11.

For PLA, the untreated raw polymer material exhibited diffraction peaks characteristic of crystalline PLA (ICDD#00-064-1624), with an average crystallite size of about 22.3 nm. In addition, reflections were observed at 2θ = 14.79, 16.64, 19.02, and 22.30°, corresponding to the (104), (200), (203), and (211) crystallo-graphic planes, respectively. In the thermally processed PLA film, these characteristic reflections were no longer clearly visible indicating that the crystallinity of the material strongly decreased after processing. In the PLA-C_{60} composite film, additional reflections assignable

to cubic C_{60} became visible, including the main peaks corresponding to the (111), (220), and (311) planes.

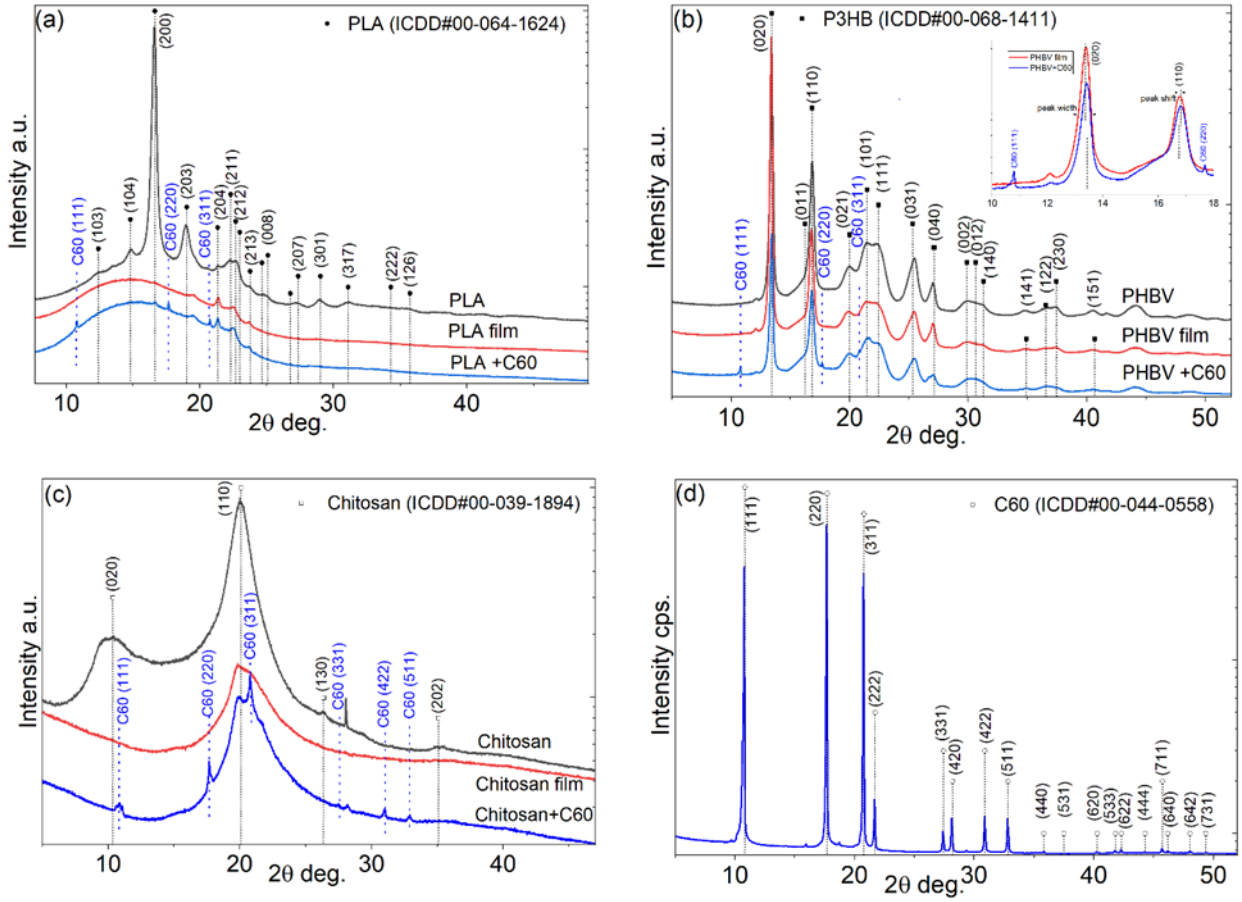

Figure 11. XRD patterns of untreated raw materials of PLA (a), PHBV (b), and chitosan (c) polymers, as well as of thermally processed films and composite films obtained by mechanical incorporation of C_{60}. (d) XRD pattern of buckminsterfullerene (C_{60}) powder mechanically incorporated into PLA, PHBV, and chitosan polymer films.

For PHBV, the raw polymer granules displayed diffraction peaks consistent with a crystalline P3HB-type structure (ICDD#00-068-1411), with the most intense reflections observed at 2θ = 13.43, 16.84, 19.98, and 25.32°, corresponding to the (020), (110), (021), and (031) crystallographic planes.

After thermal processing and film formation, the neat PHBV film retained the same main crystalline reflections. In the PHBV-C_{60} composite, these peaks remained present, while the (020) and (110) reflections shifted slightly toward higher 2θ values. The shift of the main PHBV reflections toward higher 2θ values corresponded to small decreases in the calculated a and b lattice parameters, from 5.767 to 5.747 Å and from 13.213 to 13.168 Å, respectively, while the c parameter remained constant at 5.958 Å. The crystallite size increased from 7.6 nm in the neat film to 9.2 nm in the composite. Characteristic C_{60} reflections were also present.

For chitosan, the raw material exhibited the characteristic diffraction pattern of semi-crystalline chitosan, whereas the processed neat film showed a substantial reduction in crystallinity, with only the most intense reflection at $2\theta = 20.04°$, assigned to the (110) plane, remaining clearly visible. In the chitosan-C_{60} composite, multiple characteristic C_{60} reflections were observed, and these were more numerous and more intense than in the corresponding PLA-C_{60} and PHBV-C_{60} films. Phase identification assigned the raw chitosan material to chitosan (ICDD#00-039-1894) and the fullerene-related reflections in the composite films to buckminsterfullerene C60 (ICDD#00-044-0558).

Overall, thermal processing reduced crystallinity in PLA and chitosan, while PHBV retained its crystalline structure. C_{60}-related reflections were observed in all composite films.

3.3. Effect of C_{60} incorporation on the thermal behaviour of biopolymer films

The DSC thermograms of the first heating cycle of neat polymers and their C_{60}-containing composite films are shown in Figure 12. Additional DSC data are provided in Appendix A. Distinct differences between neat and composite samples were observed for chitosan, PHBV, and PLA, indicating that C_{60} incorporation affected the thermal behaviour of all three polymer systems.

In PLA thermograms, (Figure 12a), neat PLA film exhibited an enthalpy relaxation peak associated with the glass transition at 59 °C, which has decreased in the PLA-C_{60} film, appearing at 55 °C as a sharper peak with larger peak area. In the composite, a pronounced cold-crystallisation peak was observed at 105 °C. Both neat PLA and PLA-C_{60} also displayed a crystal reorganization-related event at approximately 112 °C. In the melting region, neat PLA exhibited three melting peaks at 141 °C, 151 °C, and 161 °C, while the PLA-C_{60} film showed two main melting peaks at 144 °C and 153 °C. Compared with neat PLA, the thermal events in the composite appeared sharper and the highest-temperature melting peak was no longer observed.

In the PHBV thermograms, (Figure 12b), neat PHBV film exhibited two main melting peaks at 142 °C and 155 °C. In the PHBV-C_{60} film, the corresponding melting peaks had shifted to 148 °C and 156 °C, respectively. In addition, the composite film showed an extra melting-related peak at 167 °C, which was absent in neat PHBV. The melting region of the composite also appeared to have a larger total peak area than that of the neat polymer. Detailed thermal parameters are shown in Table A1.

In the chitosan thermograms, (Figure 12c), both samples exhibited a broad low-temperature endothermic event. For neat chitosan, the maximum of this event occurred at 109.5 °C, whereas in the chitosan-C_{60} film the corresponding peak maximum shifted to 123 °C. The broad endothermic event observed for chitosan-based films is likely associated with water loss and/or residual solvent

evaporation. The shift to higher temperature in the chitosan-C_{60} film may indicate altered water binding or changes in the hydrogen-bonding network. The endothermic event in the composite film also appeared broader and more intense than in neat chitosan. At higher temperatures, the thermogram of chitosan-C_{60} also differed from that of neat chitosan, showing an earlier deviation in the final part of the scan. Detailed thermal parameters are shown in Table A2.

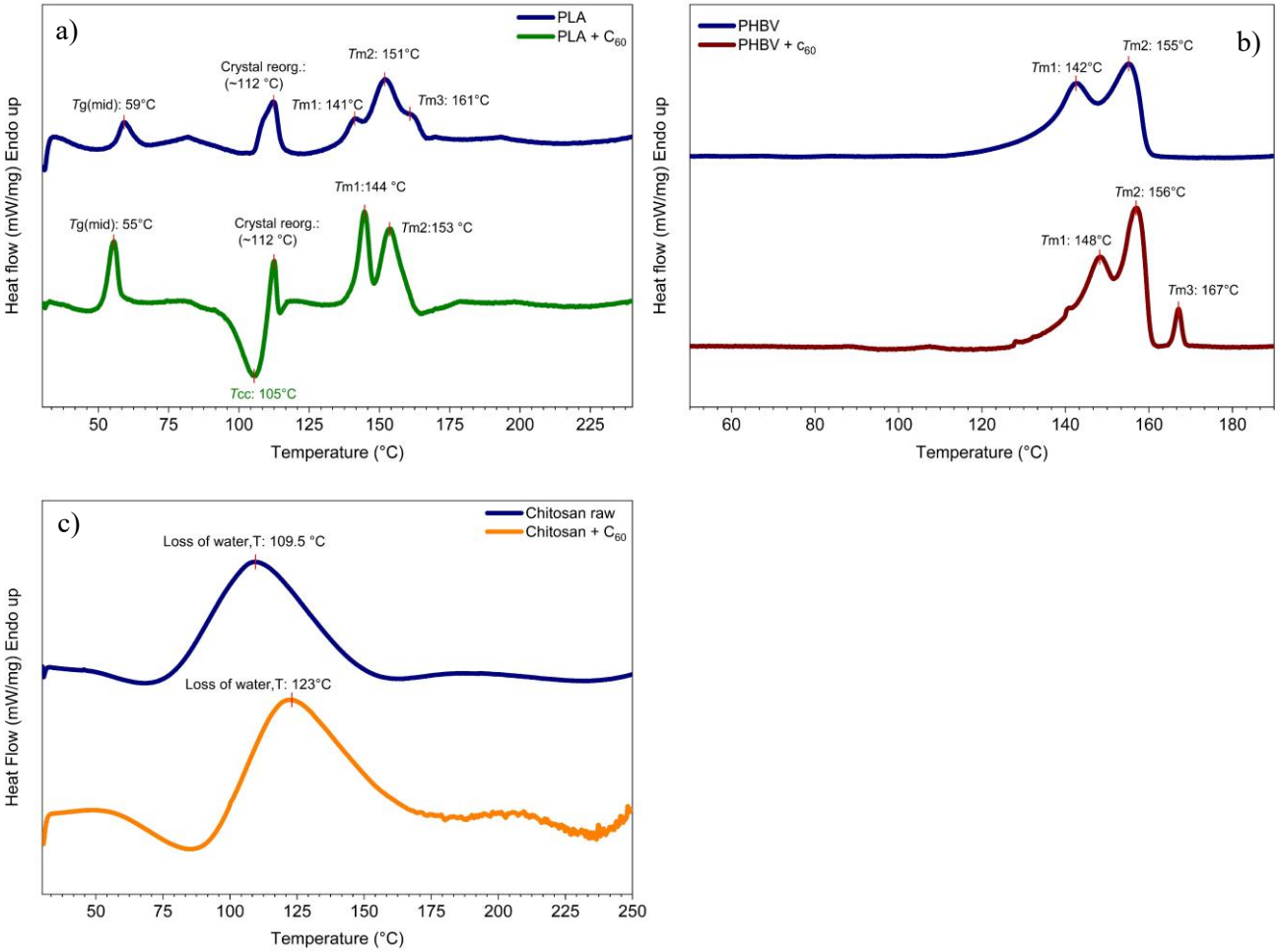

Figure 12. Differential scanning calorimetry (DSC) thermograms from the first heating cycle of neat polymer films and their C_{60}-based composite films: (a) PLA and PLA-C_{60} films, (b) PHBV and PHBV-C_{60} films, and chitosan and chitosan-C_{60} films (c). Endothermic heat flow is plotted upward.

Overall, the DSC results showed that incorporation of C_{60} altered the thermal response of all three polymer matrices, with matrix-dependent effects on the position and profile of the main thermal transitions.

3.4. Study of light-induced ROS generation by C_{60}-containing films

Reactive oxygen species generation by the prepared C_{60}-containing polymer films was quantified after 2 h of visible light irradiation using the DPA probe assay described in the Methods section.

All tested composite films produced measurable amounts of ROS. To compare the ROS-generating capacity of the materials, ROS production was normalized to the amount of C_{60} present in each sample. This normalization showed clear polymer-dependent differences in photoactivity, with ROS yields of 710.8 µmol g^{-1} C_{60} for PLA-C_{60}, 344.9 µmol g^{-1} C_{60} for PHBV-C_{60}, and 86.8 µmol g^{-1} C_{60} for chitosan-C_{60} (Figure 13). These results indicate that ROS generation followed the order PLA-C_{60} > PHBV-C_{60} > chitosan-C_{60} under the applied irradiation conditions.

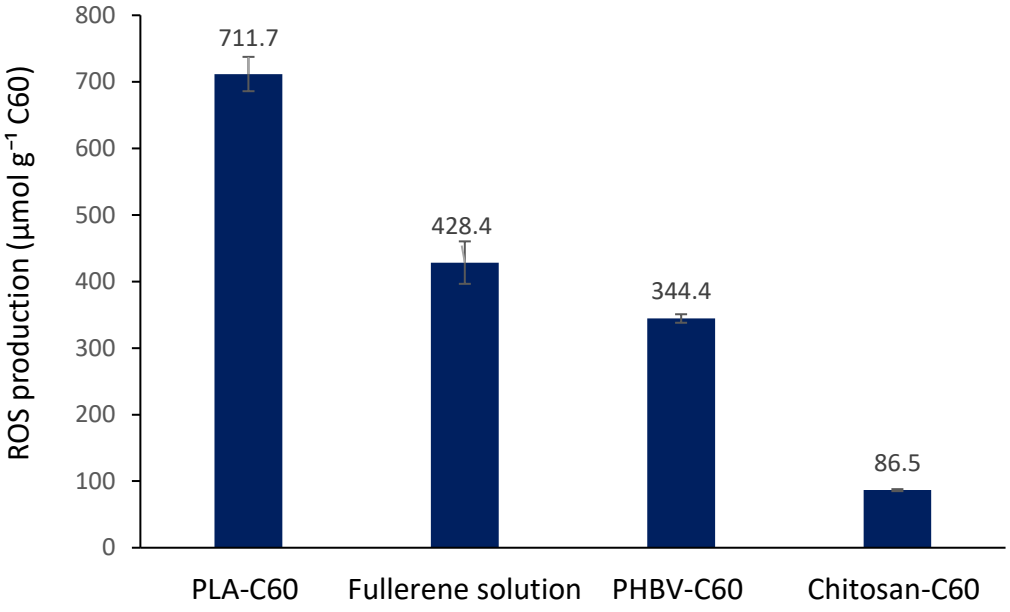

Figure 13. Relative efficiency of ROS generation per gram of C60 for C60-containing polymer films. Values are presented as mean ± standard deviation (n = 3).

In summary, all C_{60}-containing films generated measurable ROS under visible light irradiation, with PLA–C_{60} showing the highest photoactivity under the applied conditions.

3.5. Study of antimicrobial photodynamic activity of C_{60}-containing films against *S. aureus*

CFU results from both assay designs are presented in Figure 14 to allow comparison between photoirradiation during bacterial attachment and photoirradiation after bacterial attachment.

3.5.1. Photoirradiation during bacterial attachment

This assay evaluated the viability of attached *S. aureus* cells recovered from film surfaces after blue light exposure during the bacterial attachment phase (Figure 14). CFU analysis showed a marked decrease in viable *S. aureus* counts on C_{60}-containing composite films exposed to blue light compared with their corresponding dark controls.

The greatest reduction was observed for PLA-C_{60}, where bacterial counts decreased from 6.76 $\log_{10}$ CFU/mL under dark conditions to 4.10 $\log_{10}$ CFU/mL following light exposure. This corresponded to a 2.66 -$\log_{10}$ reduction. PHBV-C_{60} showed a comparable response, with viable counts decreasing from 6.51 to 4.22 $\log_{10}$ CFU/mL after illumination, equivalent to a 2.29 -$\log_{10}$ reduction. A similar trend was observed for chitosan-C_{60} films, where light exposure reduced bacterial recovery from 6.73 to 4.19 $\log_{10}$ CFU/mL, corresponding to a 2.54 -$\log_{10}$ reduction.

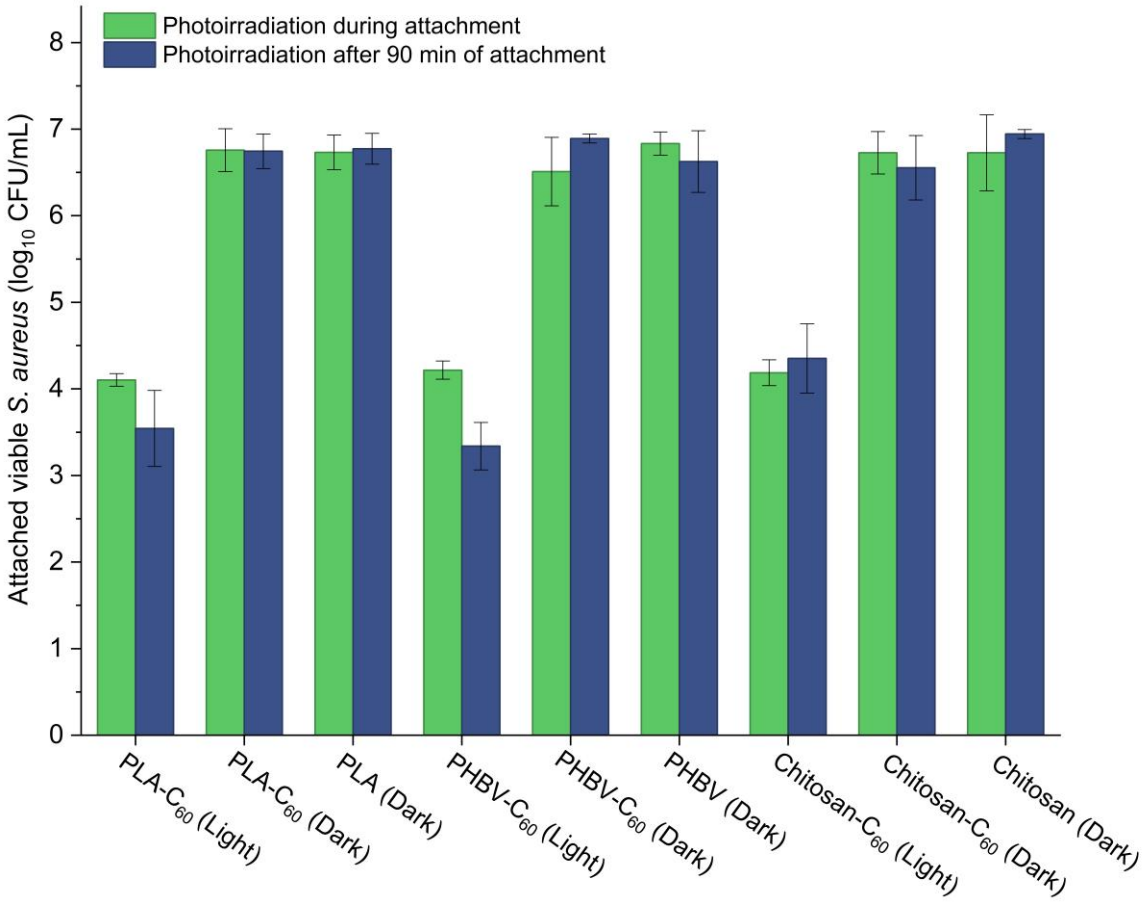

Figure 14. Attached viable *S. aureus* recovered from neat and C_{60}-containing polymer films under light and dark conditions. Green bars represent photoirradiation during the attachment phase, while blue bars represent photoirradiation after 90 min of bacterial attachment. Results are expressed as $\log_{10}$ CFU/mL. Error bars represent standard deviation

The neat polymer films also supported high bacterial recovery under dark conditions, with counts of 6.73, 6.83, and 6.73 $\log_{10}$ CFU/mL for PLA, PHBV, and chitosan, respectively. These values were comparable to those observed for the C_{60}-containing films under dark conditions, indicating that neither the polymer matrices nor the composites substantially reduced attached *S. aureus* in the absence of light activation.

Overall, the results show that C_{60}-containing films, particularly PLA-C_{60}, were able to reduce viable *S. aureus* persistence on the surface when illumination was applied during the initial bacteria–material contact period.

3.5.2. Photoirradiation of pre-attached surface-associated cells

This assay evaluated whether blue light activation of C_{60}-containing films could reduce the viability of *S. aureus* cells that had already attached to the film surface during a 90 min attachment period (Figure 14). Compared with the corresponding dark controls, all illuminated C_{60}-containing composites showed a pronounced decrease in recoverable viable cells, indicating effective photoinactivation of pre-attached bacteria.

The strongest reduction was observed for PHBV-C_{60}. Viable bacterial counts decreased from 6.89 $\log_{10}$ CFU/mL under dark conditions to 3.34 $\log_{10}$ CFU/mL after light exposure, corresponding to a 3.55 -$\log_{10}$ reduction. PLA-C_{60} also showed substantial antibacterial activity, with counts decreasing from 6.75 to 3.54 $\log_{10}$ CFU/mL, equivalent to a 3.21 -$\log_{10}$ reduction. For chitosan-C_{60} films, light exposure reduced bacterial recovery from 6.55 to 4.35 $\log_{10}$ CFU/mL, corresponding to a 2.2 -$\log_{10}$ reduction.

The neat polymer films maintained high bacterial counts under dark conditions, with values of 6.77, 6.63, and 6.94 $\log_{10}$ CFU/mL for PLA, PHBV, and chitosan, respectively. These values were comparable to those observed for the C_{60}-containing films kept in the dark, indicating that neither the polymer matrices nor the fullerene-containing composites substantially reduced attached *S. aureus* in the absence of light activation. Overall, these results suggest that blue light exposure effectively reduced the viability of pre-attached *S. aureus* on C_{60}-containing composite films, with the strongest effect observed for PHBV-C_{60} under these assay conditions.

Overall, the results indicate that C_{60}-mediated photoactivation also affected pre-attached *S. aureus* populations, with PHBV-C_{60} showing the strongest reduction in recoverable surface-associated cells under the tested conditions.

3.5.3. Metabolic activity of recovered surface-attached cells

The metabolic activity of surface-associated *S. aureus* recovered from the film surfaces was evaluated using the XTT assay (Figure 15). After treatment, the films were washed to remove non-attached cells, and the remaining surface-associated bacteria were recovered into PBS before XTT analysis. Therefore, the assay reflects the metabolic activity of bacteria that remained attached to the film after the respective light or dark treatment, rather than the activity of the initial planktonic inoculum.

XTT absorbance values were blank-corrected and normalized separately for each polymer system and assay design. The corresponding neat polymer film kept in the dark was set as 100% metabolic activity. This normalization was used to compare the C_{60}-containing films with the same polymer matrix without fullerene. Therefore, C_{60}-containing films kept in the dark indicate the effect of fullerene incorporation without light activation, while illuminated C_{60}-containing films indicate the combined effect of fullerene and photoirradiation.

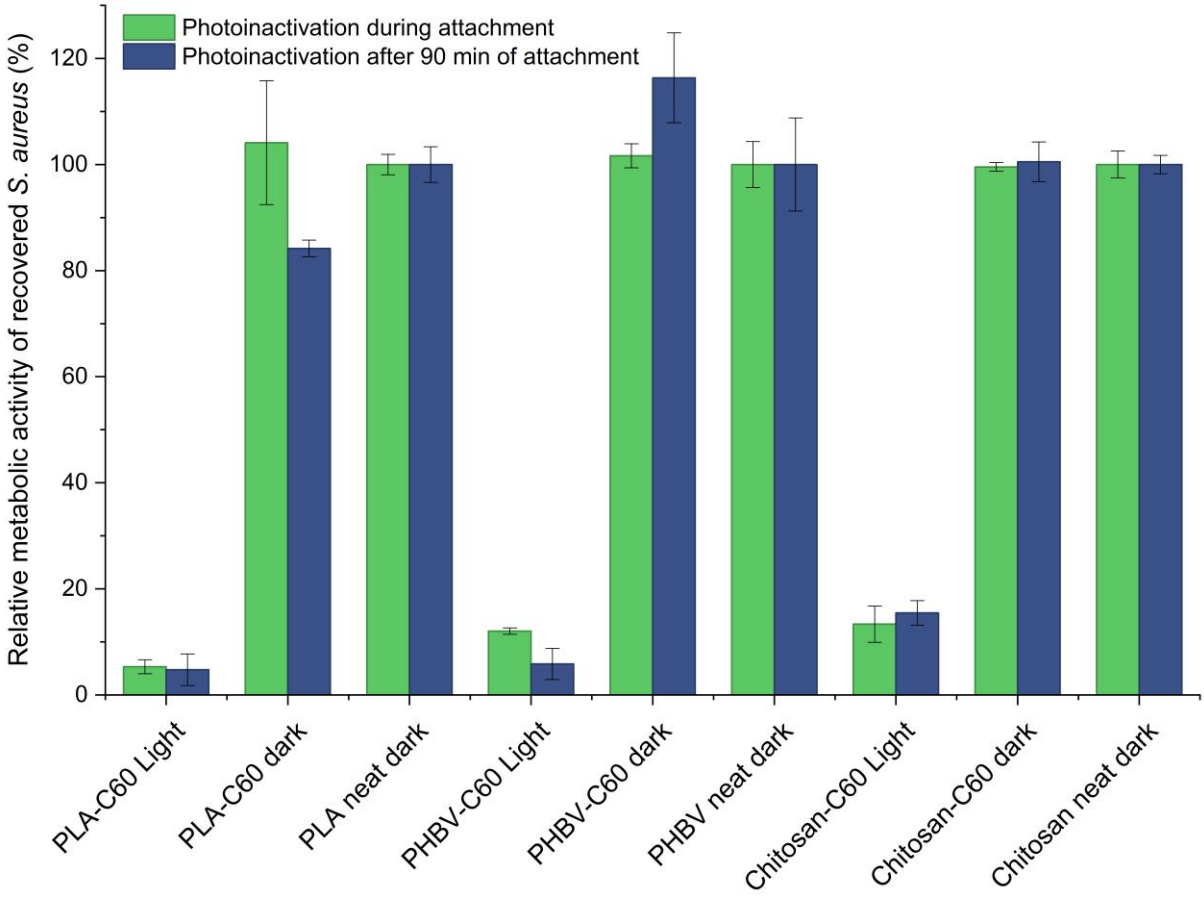

Figure 15. Relative metabolic activity of recovered *S. aureus* after XTT assay following photoirradiation during bacterial attachment and photoirradiation after 90 min pre-attachment. Values were blank-corrected and normalized to the corresponding neat polymer film kept in the dark, which was set as 100% metabolic activity. C_{60}-containing films kept in the dark were used to assess the effect of fullerene incorporation without light activation, while illuminated C_{60}-containing films were used to assess the combined effect of fullerene and photoirradiation. Error bars represent SD from three independent experimental days. Values above 100% indicate higher metabolic activity relative to the corresponding neat polymer control

During photoirradiation applied immediately during bacterial attachment, all illuminated C_{60}-containing films showed strongly reduced metabolic activity compared with the corresponding neat polymer controls. PLA-C_{60} light showed the lowest metabolic activity, decreasing to 5.33 ± 1.33%. PHBV-C_{60} light and chitosan-C_{60} light showed relative metabolic activities of 12.04 ± 0.59% and 13.35 ± 3.43%, respectively. In contrast, C_{60}-containing films kept in the dark remained close to the

neat polymer controls, with relative metabolic activity values of 104.12 ± 11.68% for PLA-C_{60}, 101.66 ± 2.27% for PHBV-C_{60}, and 99.55 ± 0.81% for chitosan-C_{60}.

A similar pattern was observed when photoirradiation was applied after 90 min of bacterial attachment. PLA-C_{60} light and PHBV-C_{60} light showed strong reductions in metabolic activity, decreasing to 4.76 ± 2.97% and 5.85 ± 2.95%, respectively. Chitosan-C_{60} light showed a weaker but still clear reduction, with relative metabolic activity of 15.46 ± 2.30%. C_{60}-containing films kept in the dark showed substantially higher metabolic activity than illuminated samples, with values of 84.17 ± 1.59% for PLA-C_{60}, 116.35 ± 8.47% for PHBV-C_{60}, and 100.52 ± 3.75% for chitosan-C_{60}.

Overall, the XTT results support the CFU findings by showing that blue light activation of C_{60}-containing films strongly reduced the metabolic activity of recovered surface-associated *S. aureus*. The C_{60}-containing dark controls remained close to the corresponding neat polymer controls, indicating that fullerene incorporation alone did not cause a consistent decrease in metabolic activity in the absence of light. Therefore, the reduction observed in illuminated C_{60}-containing films was mainly associated with light activation of incorporated C_{60}.

3.5.4. Scanning Electron Microscopy (SEM)

SEM analysis was performed to qualitatively assess the presence and distribution of *S. aureus* cells remaining on the film surfaces after bacterial attachment, blue-light irradiation, and repeated PBS washing. Representative SEM micrographs are shown in Appendix B.

Neat PLA, PHBV, and chitosan films showed visible retention of coccoid bacterial cells after the treatment procedure. The cells were observed either as isolated cells or as small surface-associated clusters. Among the neat materials, chitosan showed the most extensive visible bacterial coverage, with dense areas of retained cells and aggregates. PLA and PHBV also showed retained cells, although the distribution was more dispersed.

In contrast, the corresponding films containing 0.5% C_{60} showed a visibly lower number of retained bacterial cells. This reduction was particularly evident for PLA + 0.5% C_{60} and PHBV + 0.5% C60, where only sparse individual cells or small residues were observed across the imaged areas. Chitosan + 0.5% C_{60} also showed reduced bacterial coverage compared with neat chitosan, although scattered cells and irregular surface-associated residues remained visible.

Overall, the SEM images indicate that incorporation of 0.5% C_{60} was associated with reduced visible bacterial retention on all three polymer films following blue-light exposure and washing. These observations support the use of SEM as qualitative morphological evidence of differences in surface-associated bacterial presence between neat and fullerene-containing films.

4. Discussion

The aim of this work was to fabricate fullerene C_{60}-containing biopolymer films and evaluate whether these materials could function as light-activated antimicrobial surfaces against *Staphylococcus aureus*. The work addressed four linked objectives: 1) preparation of PLA, PHBV, and chitosan films containing C_{60}; 2) confirmation of C_{60} incorporation and its effects on polymer structure; 3) assessment of light-induced reactive oxygen species (ROS) generation by composite films; and 4) evaluation of antimicrobial photodynamic activity against *S. aureus*. Overall, the findings support the central hypothesis that C_{60} can be incorporated into biopolymer matrices by thermomechanical or hot-pressing routes while retaining photoactive functionality. Additionally, the results show that the polymer matrix strongly determines C_{60} distribution, thermal behaviour, ROS output, and biological performance. Therefore, the antimicrobial activity observed in this study should not be interpreted as a property of C_{60} alone, but as an outcome of the combined C_{60}-polymer-light-bacteria interface.

4.1. Fabrication feasibility and material integrity

All three biopolymer systems (PLA, PHBV, chitosan) were successfully processed into neat and C_{60}-containing films, although the processing parameters required adjustment according to polymer-specific thermal and rheological behaviour. This suggests that the selected fabrication approaches are compatible with fullerene incorporation across chemically distinct biopolymer matrices, fulfilling the first objective of this work. The need for system-specific processing conditions indicates that matrix-dependent chain mobility and thermal stability govern film formation, which is consistent with established differences in melt-processable polyesters versus solution-processed polysaccharides (e.g., PLA/PHBV vs chitosan). For example, PLA has a relatively stable processing window compared to other biopolyesters. It softens and flows at moderate temperatures (typically 160–190 °C), allowing conventional extrusion, injection moulding and thermoforming (Tao et al., 2024). However, when exposed to high temperatures or long residence times, PLA undergoes chain scission and hydrolysis that reduce its molecular weight and viscosity (Velghe et al., 2023). In contrast, PHBV presents a much narrower thermal processing window. Its melting temperature (165–175 °C) nearly coincides with the onset of thermal degradation, so small deviations in processing conditions can trigger chain rupture and viscosity loss (Zembouai et al., 2013). Although processing remains sensitive due to the narrow thermal stability range and risk of degradation, the extensive prior research on these polymers provided established guidelines, making parameter selection more controlled and manageable.

Chitosan, on the other hand, is generally not melt-processable by itself due to its low thermal stability and poor melt flow (Merijs-Meri et al., 2024). This means that pure chitosan tends to degrade

and lose molecular weight when subjected to typical melt-processing conditions, leading to poor processability and deteriorated mechanical properties if processed alone (Merijs-Meri et al., 2024). However, when plasticizers, such as glycerol, sorbitol or water are added, the melting temperature can be substantially reduced (Matet et al., 2013). For this reason, glycerol and water were selected as plasticizers in this work, as their ability to reduce effective processing temperature is well-documented, especially in chitosan systems for films and biodegradable materials (Epure et al., 2011; Leceta et al., 2013; Matet et al., 2013). Melt-processed chitosan is surprisingly widely investigated for functional food packaging and biomedical applications, such as composites for tissue regeneration (Correlo et al., 2010, 2016; Janik et al., 2021).

Together, these differences show that tuning processing to each polymer's nature is key to producing stable, C_{60}-based biopolymer films suited for antimicrobial coatings.

4.2. Fullerene incorporation and structural preservation

Raman spectroscopy confirmed the presence of C_{60} in all composite films through characteristic vibrational modes, including the Ag (2) band at ~1467 cm^{-1} and additional Hg modes (Dorner-Reisel et al., 2022; Qin et al., 2025). The absence of peak shifts indicates that the fullerene molecular structure remained intact during both processing and laser exposure (Yao et al., 2013; Yun-Chong & Yun-Fan, 2010). This is a critical result, as preservation of the π-conjugated structure of C_{60} is directly linked to its ability to generate reactive oxygen species (ROS) under light irradiation (Mroz et al., 2007).

This observation aligns with previous reports showing that fullerene retains its photophysical properties when embedded in polymer matrices, provided no strong covalent interactions occur. Philips et al. studied non-covalently blended C_{60}-polymer adhesive nanocomposites, where C_{60} was physically incorporated into polystyrene-block-polybutadiene-block-polystyrene (SBS) and polystyrene-block-polyisoprene-block-polystyrene (SIS) PSA films (Phillips et al., 2008). They showed that C_{60} retained photosensitizing activity in the films, as demonstrated by oxygen-dependent, light-induced adhesive loss that was suppressed by the singlet oxygen quencher β-carotene (Phillips et al., 2008). Another study suggested that in addition to ROS generation, such photoactive fullerene-containing polymer materials can also induce damage to biological systems (McCluskey et al., 2009).

While photoactive antimicrobial polymers containing C_{60} have not yet been extensively developed through melt processing, related research suggests that this method is viable. Wylie et al. demonstrated that antimicrobial polymer surfaces containing the photosensitizer toluidine blue O (TBO) could be produced by hot-melt extrusion (Wylie et al., 2021). TBO remained stable up to 230 °C, could be incorporated into several medical polymer classes, and produced a statistically significant reduction in *S. aureus* viability after 4 h of irradiation (Wylie et al., 2021). In view of this, pristine

C_{60} has been reported to withstand temperatures up to approximately 714 °C under inert atmosphere, supporting its thermal robustness during melt processing (Nikonova et al., 2021). Pereira et al. demonstrated that C_{60} could be integrated into polyethylene through melt processing, and even at loadings as low as 1.0 wt%, the thermo-oxidative stability of the resulting nanocomposites was significantly enhanced (Pereira et al., 2015).

Collectively, these findings demonstrate that C_{60} retained its characteristic molecular structure after composite processing, supporting the interpretation that the developed biopolymer-C_{60} films preserved the structural basis required for photodynamic activity.

4.3. Dispersion and spatial distribution of C_{60}

Optical microscopy and Raman mapping revealed that C_{60} was not molecularly or uniformly dispersed in any of the investigated polymer matrices. Instead, the Raman maps constructed from the 1467 cm^{-1} fullerene band showed discrete C_{60}-rich domains, with the fullerene phase occupying approximately 10–15% of the scanned area. This result suggests that while melt processing may have lessened the dependence on solvent-mediated incorporation, it did not entirely eliminate the inherent tendency of pristine C_{60} to self-associate within polymer matrices.

The extent of heterogeneity was matrix-dependent. PLA showed the highest local Raman intensity, with a maximum Ag (2) signal of 10,500 counts, almost one order of magnitude higher than chitosan and PHBV. This suggests that C_{60} was likely concentrated into fewer, highly enriched domains in PLA, consistent with the formation of fullerene agglomerates or phase-segregated islands (Falke et al., 2011; Qin et al., 2025). In contrast, chitosan and PHBV showed lower maximum intensities of 1450 and 1000 counts, respectively, suggesting less severe local enrichment of C_{60}. Although such heterogeneity is undesirable from a dispersion perspective, it may enhance apparent ROS generation by increasing local photon absorption in fullerene-rich regions (Kang et al., 2021). Such local photon concentration increases the likelihood of fullerene photoexcitation and might boost ROS generation. This effect is similar in principle to the enhanced photogeneration of ROS observed in other heterostructured nanomaterials, where spatial separation and structuring lead to improved light harvesting and charge carrier dynamics (Kang et al., 2021).

In this context, the high ROS yield observed for PLA-C_{60} may be partly related to the presence of fullerene-rich domains, as this composite showed an almost 1.6-fold higher ROS yield than C_{60} in solution under the same assay conditions. A similar trend was reported by Soon et al., who found that polymer/fullerene blend films generated significantly more singlet oxygen than the corresponding solution-only control (Soon et al., 2013). For photosensitizers, aggregation often reduces activity because it can promote self-quenching (Speller et al., 2017). However, fullerene photochemistry is more morphology dependent, and a lot depends on aggregate size, packing, oxygen accessibility, and film

morphology. Speller et al. showed that fullerene film photochemistry depends strongly on nanomorphology (Speller et al., 2017). More dispersed fullerene/polymer blends were more susceptible to oxygen quenching and photobleaching than more aggregated fullerene films (Speller et al., 2017). This might help explain why PHBV and chitosan composite films showed lower ROS generation capacity than PLA and C_{60} in a solution, despite the less severe fullerene aggregation in the matrix.

4.4. Polymer-dependent structural interactions (XRD and DSC integration)

The matrix-dependent behaviour observed in Raman mapping was also reflected in the XRD and DSC results. Together, these analyses suggest that PLA, PHBV, and chitosan created different structural environments for C_{60} incorporation, influencing crystallinity, thermal transitions, and overall composite organization.

For PLA, both XRD and DSC indicated reduced crystallinity and the presence of cold crystallization. DSC data suggested that C_{60} likely acts as a nucleating agent that promotes cold crystallization. The disappearance of the highest-temperature melting peak (~160 °C) in the PLA-C_{60} film, combined with sharper and more defined melting events, indicates suppression of large, well-developed α crystals and preferential formation of smaller, more uniform α′ crystallites. The appearance of a cold-crystallization peak in PLA-C_{60} suggests that C_{60} modifies the crystallization behaviour of PLA, possibly by acting as a heterogeneous nucleation site during heating. However, because the calculated initial crystallinity remains low, this effect should be interpreted as a change in crystallization kinetics rather than as a clear increase in the final crystalline fraction. These thermal observations are consistent with the XRD results, which showed reduced long-range order indicative of smaller and less perfect crystallites rather than a fully amorphous structure. Studies on PLA nanocomposites show that refined crystal structures can improve surface uniformity and reduce localized wear, especially under mild abrasion conditions (Gao & Masato, 2024; Tang et al., 2012).

For PHBV, the XRD and DSC results suggest a different response to C_{60} incorporation. Unlike PLA, PHBV retained its main crystalline structure after processing. The slight lattice contraction, increase in crystallite size, higher melting temperatures, and small increase in crystallinity all point towards a more ordered crystalline structure in the composite. Therefore, C_{60} may have contributed to the formation or stabilization of more stable PHBV crystalline regions. The additional melting peak at 167 °C supports this interpretation, as it may be related to thicker or more stable lamellae. Functionally, these properties could be associated with increased stiffness, strength and modulus (Dusunceli & Colak, 2008) which in turn means that the resulting composite films are more wear-resistant and durable (Tóth et al., 2019).

For chitosan, XRD indicates reduced crystallinity after processing and strong, distinct C_{60} reflections, suggesting that fullerene remains as a separate crystalline phase with limited dispersion.

Although DSC data are dominated by water-related transitions rather than classical melting behaviour, the observed shift of the endothermic peak to higher temperature indicates stronger water binding and altered hydrogen-bonding interactions.

A plausible interpretation of these results is that the processing disrupted the native hydrogen-bonded structure of chitosan, while C_{60} was not fully integrated into the polymer matrix and primarily remained as separate crystalline domains. Because of this, C_{60} is unlikely to act as a reinforcing component in chitosan films. Instead, it appears to increase structural heterogeneity, which may contribute to lower mechanical strength and reduced resistance to abrasion or surface wear. At the same time, the high flexibility of chitosan-C_{60} films may be beneficial for applications on soft or irregularly shaped surfaces, where more rigid PLA- or PHBV-based films may be less suitable. However, because the thermal behaviour of these films is strongly affected by bound water, their mechanical and thermal stability is expected to depend strongly on humidity, which could limit their reliability under variable environmental conditions.

Antimicrobial coatings for long-term use on clinical or high-touch surfaces must retain function after repeated cleaning, abrasion, and handling. Durability depends on formulation, substrate condition, and wear exposure, and some coatings lose coverage or activity after limited abrasion cycles(Buhl et al., 2020). In healthcare, repeated cleaning is unavoidable; thus, antimicrobial coatings should complement standard hygiene practices, not replace them(Bäumler et al., 2022).

Considering these requirements, PHBV-C_{60} appears to be the strongest candidate for mechanically demanding antimicrobial surfaces, as its structural response suggests a relatively stable crystalline matrix that may better withstand deformation and surface wear. PLA-C_{60} also shows potential, particularly for less demanding surfaces where improved homogeneity may help reduce localized wear. However, its lower crystallinity and cold-crystallization behaviour make its long-term durability less predictable. Considering all, chitosan-C_{60} shows the least potential for such application because its heterogeneous, water-sensitive structure is likely to be more vulnerable to abrasion and humidity changes. Nevertheless, its flexibility may make it relevant for soft, curved, or irregular interfaces where conformability is more important than mechanical durability.

Overall, these matrix-dependent structural differences provide an important basis for interpreting the antimicrobial results. In solid C_{60}-containing films, antibacterial activity is not determined only by the amount of fullerene present, but also by how the polymer matrix affects fullerene distribution, exposure to light and oxygen, and contact with surface-associated bacteria. Thus, the different antimicrobial responses of PLA-C_{60}, PHBV-C_{60}, and chitosan-C_{60} are likely linked to the distinct structural environments created by each polymer matrix.

4.5. Photochemical and antimicrobial activity

4.5.1. Capacity of biopolymer-C_{60} composite films to generate ROS

The photochemical and microbiological results show that incorporating C_{60} into the biopolymer films produced light-activated antibacterial surfaces, but the strength of this effect depended strongly on the polymer matrix. Fullerene-based photosensitizers can generate singlet oxygen through a Type II photodynamic pathway and other reactive species through Type I electron-transfer processes, both of which may contribute to antimicrobial photodynamic inactivation (Hou et al., 2022). Under blue-light irradiation, C_{60} is generally associated mainly with singlet oxygen formation, although the balance between different ROS pathways depends on the surrounding medium, oxygen availability, aggregation state, and matrix interactions (Mroz et al., 2007). Since DPA was the only probe used in this study, the assay supports singlet oxygen generation but does not define the full ROS profile. Therefore, possible contributions from Type I ROS to the antibacterial effect cannot be excluded.

All C_{60}-containing films generated detectable singlet oxygen under irradiation, indicating that thermomechanical incorporation did not eliminate fullerene photoactivity in PLA, PHBV, or chitosan. However, the response differed strongly between the matrices. PLA-C_{60} produced the highest signal (711.7 μmol g^{-1} C_{60}), exceeding the fullerene solution reference tested under the same conditions (428.4 μmol g^{-1} C_{60}). PHBV-C_{60} still generated a clear signal, although lower than PLA-C_{60}, whereas chitosan-C_{60} showed only weak singlet oxygen production. Because these values were normalized to fullerene content, the differences cannot be explained by C_{60} loading alone. They more likely reflect how each matrix affected fullerene exposure, oxygen access, and interaction with the DPA probe.

The high signal of PLA-C_{60} is particularly interesting because Raman mapping and optical microscopy showed that this system had the strongest fullerene heterogeneity. PLA-C_{60} contained intense C_{60}-rich regions, suggesting stronger aggregation or phase separation than in the other films. At first, this seems inconsistent with the high ROS yield, since aggregation is often associated with self-quenching and reduced photosensitizer efficiency (Speller et al., 2017). However, in solid films this relationship is not necessarily straightforward. If fullerene-rich regions remain exposed to light and oxygen, they may still act as active photodynamic sites despite poor overall dispersion (Nyga et al., 2022). Previous studies on polymer/fullerene films also show that singlet oxygen generation depends strongly on blend morphology and excited-state behaviour, rather than on fullerene content alone (Soon et al., 2013). In addition, better-dispersed, less aggregated fullerene domains are more susceptible to oxygen quenching of triplet states and photooxidation, whereas stronger aggregation can partly shield some fullerene molecules from oxygen and reduce this interaction (Speller et al., 2017).

Therefore, the high DPA-detectable singlet oxygen signal in PLA-C_{60} may reflect not uniform dispersion, but the presence of accessible C_{60}-rich domains that remained sufficiently exposed to light and oxygen to act as active photodynamic sites.

The lower singlet oxygen generation in PHBV-C_{60} and chitosan-C_{60} suggests a different matrix effect. In PHBV, the more crystalline matrix may have restricted oxygen diffusion or reduced contact between C_{60} and the DPA probe, even though fullerene remained photoactive. In chitosan, the weak signal may be related to phase-separated C_{60} domains, water-dependent matrix structure, and poorer effective contact between fullerene, oxygen, and the probe. Thus, DPA-detectable singlet oxygen generation was not controlled simply by C_{60} content or apparent aggregation, but by how accessible and photochemically active the fullerene-rich regions were within each matrix.

Overall, the results suggest that thermomechanical processing preserved C_{60} photoactivity in all three biopolymer films, but the efficiency of singlet oxygen generation appeared to be dependent on matrix-controlled fullerene exposure. Although PLA-C_{60} generated the highest singlet oxygen equivalents in the chemical probe assay, ROS generation measured in solution does not necessarily directly reflect ROS availability at the bacteria-film interface. Therefore, antimicrobial performance likely also depended on factors such as fullerene accessibility, oxygen diffusion within the polymer matrix, bacterial contact with photoactive domains, and surface-associated ROS transport.

4.5.2. Photoactivity of biopolymer-C_{60} composite films against *S. aureus*

The microbiological assays confirmed that C_{60}-containing biopolymer films acted as light-activated antibacterial surfaces against *S. aureus*. In both assay designs, illuminated composites showed markedly lower viable cell recovery and reduced metabolic activity compared with their corresponding dark controls, whereas neat polymer films and C_{60}-containing films kept in the dark supported high bacterial recovery. This suggests that the antibacterial effect was mainly caused by light activation of incorporated C_{60} rather than by the polymer matrices alone or by dark toxicity of fullerene.

The CFU data showed activity both during the initial bacteria–surface contact period and after 90 min of attachment. Since early adhesion is the first step in biofilm development (Donlan, 2002), the reduction of recoverable attached cells suggests that these films may interfere with early biofilm establishment. This is consistent with antimicrobial photodynamic therapy, where ROS generated after photoactivation may contribute to damage of microbial cells and biofilm-associated components, including proteins, lipids, nucleic acids, and matrix material (Hu et al., 2018).

A key finding is that the two assay designs did not give the same ranking of the materials. During bacterial attachment, PLA-C_{60} showed the strongest CFU reduction, followed closely by chitosan-C_{60} and PHBV-C_{60}. After 90 min of attachment, PHBV-C_{60} showed the greatest reduction, fol-

lowed by PLA-C_{60}, while chitosan-C_{60} remained the least effective. This difference suggests that antibacterial performance was not determined by ROS generation alone. During the attachment phase, bacterial contact with the material, local ROS generation, and early adhesion processes occurred simultaneously. In the post-attachment assay, cells had already interacted with the surface before light activation, so the outcome likely depended more strongly on adhesion strength, local ROS availability at the cell–film interface, and the removal of damaged cells during washing.

The ROS and Raman mapping results may help explain these differences. PLA-C_{60} generated the highest amount of DPA-detectable singlet oxygen, which agrees with its strong antibacterial activity during the attachment-phase assay. PHBV-C_{60} produced a lower singlet oxygen signal than PLA-C_{60} yet showed the strongest CFU reduction against pre-attached cells. This suggests that the chemical DPA assay does not fully predict antibacterial performance at the cell–material interface: the more crystalline PHBV matrix may have influenced oxygen or DPA diffusion in solution, while still allowing effective local ROS action near attached bacteria. Chitosan-C_{60} showed the lowest singlet oxygen generation and the weakest antibacterial performance, suggesting that its lower ROS output, water-sensitive structure, and stronger bacterial retention limited its overall efficiency despite retained photoactivity.

The XTT assay supported the CFU results by showing that the reduction in recoverable bacteria was accompanied by a strong loss of metabolic activity. This is important because CFU enumeration reflects the ability of recovered cells to form colonies, whereas XTT provides an additional indication of metabolic impairment in the surface-associated bacterial population. Under dark conditions, the C_{60}-containing films showed metabolic activity close to the corresponding neat polymer controls, indicating that fullerene incorporation alone did not produce a consistent antibacterial effect. In contrast, illuminated C_{60}-containing films showed low residual metabolic activity in both assay designs, supporting a light-dependent mechanism. This agrees with the expected mode of antimicrobial photodynamic therapy, where photoactivated photosensitizers generate ROS that damage several cellular targets and impair bacterial viability and metabolism. The higher metabolic activity observed for PHBV-C_{60} in the dark after 90 min attachment likely reflects material- and day-dependent variation in bacterial recovery or XTT signal rather than a biologically meaningful stimulatory effect, especially because the corresponding illuminated PHBV-C_{60} samples showed one of the strongest reductions in metabolic activity. Thus, the XTT data reinforce the interpretation that C_{60}-mediated photoactivation, rather than dark toxicity, was responsible for the antibacterial response.

SEM observations provided qualitative support for the microbiological findings. Neat films showed visible retention of coccoid *S. aureus* cells after washing, while illuminated C_{60}-containing films showed fewer retained cells, especially PLA-C_{60} and PHBV-C_{60}. This supports the interpretation

that photoactivation reduced viable surface-associated bacteria and may have weakened bacterial retention.

Previous fullerene-based antimicrobial coatings have shown that immobilized C_{60} can retain photodynamic activity and generate ROS under irradiation (Reynoso et al., 2019). However, many reported systems rely on chemical functionalization, electrochemical deposition, or solution-based coating methods. In contrast, the present work shows that C_{60}-mediated photoactivity can be preserved after thermomechanical processing in biodegradable polymer matrices.

4.6. Limitations and future perspectives

The main limitations of this study should also be acknowledged. ROS generation was measured using a chemical probe in solution, which may not fully reflect how much ROS is available directly at the bacteria–film interface. In addition, the cells removed during washing were not quantified separately, so the assays mainly describe the bacteria that remained associated with the film surface after treatment. SEM observations were also qualitative, and the long-term stability of the films, repeated irradiation cycles, and possible C_{60} leaching were not evaluated. Therefore, although the results show clear light-dependent antibacterial activity, further studies are needed to assess the durability, reusability, and performance of these films under more clinically relevant conditions.

From an application perspective, PLA-C_{60} and PHBV-C_{60} appear to be the more suitable candidates for further development as solid surface-based antimicrobial coatings. Both matrices showed better thermomechanical processability than chitosan and retained clearer film integrity after processing, while PHBV-C_{60} also showed favourable structural stability in XRD and DSC analysis. These properties make PLA- and PHBV-based systems more relevant for future development of durable photoactive coatings for medical-device or food-contact surface applications. In contrast, chitosan-C_{60} remained photoactive but showed weaker antimicrobial performance and lower structural stability as a solid pressed film. Therefore, chitosan may be more suitable for future solution-based or spray deposited coating strategies, where its film-forming ability, biodegradability, and antimicrobial background can be combined with improved photosensitizer dispersion. This direction is consistent with further work aimed at developing electrosprayed photoactive nanoparticle coatings, such as fullerene-based particles functionalized with 5-aminolevulinic acid and embedded in a sustainable chitosan matrix.

In summary, this study demonstrates that unmodified C_{60} can retain light-activated antimicrobial function after thermomechanical incorporation into biodegradable polymer films. The antibacterial performance of the films was material-dependent and could not be predicted solely from total ROS generation, indicating that fullerene distribution, polymer morphology, and bacterial–surface interactions jointly control the efficiency of surface-based aPDT.

Conclusions

PLA-, PHBV-, and chitosan-based films containing 0.5 wt% C_{60} were successfully prepared. PLA and PHBV were processed by extrusion, injection moulding, and hot pressing, whereas chitosan films were obtained by hot pressing after manual premixing.

Raman spectroscopy confirmed C_{60} incorporation in all three biopolymer matrices, whereas Raman mapping showed a heterogeneous, matrix-dependent fullerene distribution. XRD and DSC analyses further showed that C_{60} affected the polymer structures differently: PHBV-C_{60} retained the most stable crystalline structure, PLA-C_{60} showed reduced crystallinity and strong fullerene heterogeneity, and chitosan-C_{60} showed pronounced C_{60}-related phase separation and water-dependent thermal behaviour.

All C_{60}-containing films generated detectable ROS under 450 nm blue-light irradiation, indicating that C_{60} retained its photoactivity after processing. ROS generation depended on the polymer matrix and followed the order PLA-C_{60} > PHBV-C_{60} > chitosan-C_{60}.

Microbiological assay results have indicated light-dependent antibacterial activity against surface-associated *S. aureus*. Illuminated C_{60}-containing films reduced both recoverable viable bacteria and metabolic activity, whereas neat films and C_{60}-containing films kept in the dark supported high bacterial recovery. PLA-C_{60} was the most effective during bacterial attachment, PHBV-C_{60} showed the strongest activity against pre-attached cells, and chitosan-C_{60} remained photoactive but was the least efficient system.

Overall, this work demonstrates that unmodified C_{60} can retain light-activated antimicrobial function after thermomechanical incorporation into biodegradable polymer films. PHBV-C_{60} showed the most favourable balance between structural stability and antibacterial performance, whereas the differences between the three systems show that fullerene distribution, ROS generation, and bacterial–surface interactions jointly determine antimicrobial efficiency.

Author contribution and acknowledgements

The research idea and overall study direction were proposed by Dr. Wanessa CMA Melo. The author contributed to the experimental design, fabricated the biopolymer–C_{60} composite films, interpreted Raman spectroscopy data, XRD and DSC data, conducted ROS measurements, performed microbiological analysis of PHBV- and chitosan-based samples, analysed the results, and wrote the thesis.

Microbiological analysis of PLA-based samples was performed in collaboration with bachelor's student Marija Tichoniuk within the same research group. The PLA films were fabricated by the author, and the resulting microbiological data were analysed and interpreted jointly.

The author would like to sincerely thank Dr. Wanessa CMA Melo supervision and scientific guidance. The author also acknowledges Dr. María Belén Montero Rodríguez for consultation and assistance during the research internship at CITENI, Dr. Martynas Talaikis for assistance with Raman spectroscopy measurements, Dr. Vidas Pakštas for assistance with XRD measurements, senior engineer Andrius Maneikis for SEM analysis performed at the Faculty of Electronics, Vilnius Gediminas Technical University, and Dr. Povilas Šimonis for support during thesis preparation and guidance in the presentation of the work.

VILNIAUS UNIVERSITETAS
GYVYBĖS MOKSLŲ CENTRAS

Guoda Gasauskaitė

Magistro baigiamasis darbas

Fotoaktyvios biopolimerų–C_{60} nanokompozitinės plėvelės bakterijų prisitvirtinimo ir ankstyvo biofilmo formavimosi slopinimui

SANTRAUKA

Su bioplėvelių susidarymu susijusios infekcijos išlieka svarbia sveikatos priežiūros problema, ypač mikroorganizmams kolonizuojant medicinos prietaisų ar dažnai liečiamus paviršius. Šviesa aktyvuojami antimikrobiniai paviršiai gali padėti kontroliuoti bakterijų prisitvirtinimą, nes reaktyviosios deguonies formos susidaro tik apšvietus fotoaktyvią medžiagą. Šiame darbe fullerenas C_{60} buvo įterptas į poli(pieno rūgšties) (PLA), poli(3-hidroksibutirato-ko-3-hidroksivalerato) (PHBV) ir chitozano plėveles, siekiant sukurti šviesa aktyvuojamus antimikrobinius biopolimerinius paviršius prieš *Staphylococcus aureus*.

PLA ir PHBV kompozitai buvo pagaminti termomechaninio apdorojimo būdu, o chitozano plėvelės - karštu presavimu. Ramano spektroskopija patvirtino C_{60} įterpimą į visas kompozitines plėveles, tačiau Ramano žemėlapiai parodė netolygų, nuo polimerinės matricos priklausantį fulereno pasiskirstymą. XRD ir DSC analizės parodė, kad C_{60} skirtingai veikė polimerų struktūrą: PHBV-C_{60} pasižymėjo didžiausiu struktūriniu stabilumu, PLA-C_{60} - ryškiausiu fulereno heterogeniškumu ir sumažėjusiu kristališkumu, o chitozano-C_{60} plėvelėse nustatytos atskiros C_{60} fazės ir nuo vandens priklausoma šiluminė elgsena.

Visos C_{60} turinčios plėvelės generavo singletinį deguonį veikiant 450 nm mėlynai šviesai, todėl buvo patvirtinta, kad fullerenas po apdorojimo išlaikė fotodinaminį aktyvumą. Didžiausias ROS signalas nustatytas PLA-C_{60} plėvelėse, mažesnis - PHBV-C_{60}, o silpniausias – chitozano-C_{60} plėvelėse. Mikrobiologiniai tyrimai parodė nuo šviesos priklausomą antibakterinį poveikį paviršiuje prisitvirtinusioms S. aureus ląstelėms: PLA-C_{60} buvo veiksmingiausia bakterijų prisitvirtinimo metu, PHBV-C_{60} labiausiai sumažino jau prisitvirtinusių ląstelių kiekį, o chitozano-C_{60} poveikis buvo silpniausias.

Apibendrinant, termofiziškai apdorotos C_{60} turinčios biopolimerinės plėvelės gali veikti kaip šviesa aktyvuojami antimikrobiniai paviršiai, tačiau jų veiksmingumas priklauso nuo polimerinės matricos, fulereno pasiskirstymo, ROS generacijos ir bakterijų sąveikos su paviršiumi.

VILNIUS UNIVERSITY
LIFE SCIENCES CENTER

Guoda Gasauskaitė

Master's thesis

Photoactive Biopolymer–C60 Nanocomposite Films for Biofouling Resistance

ABSTRACT

Biofilm-associated infections remain a major healthcare problem, particularly in medical devices and high-touch surfaces. Antimicrobial photodynamic surfaces offer a potential strategy for controlling bacterial attachment because they generate reactive oxygen species only after light activation. In this study, fullerene C_{60} was incorporated into poly (lactic acid) (PLA), poly(3-hydroxybutyrate-co-3-hydroxyvalerate) (PHBV), and chitosan films to develop light-activated antimicrobial biopolymer surfaces against Staphylococcus aureus.

PLA and PHBV composites were prepared by thermomechanical processing, whereas chitosan films were fabricated by hot pressing after manual premixing with C_{60} and plasticisers. Raman spectroscopy confirmed C_{60} incorporation in all films; however, Raman mapping showed that fullerene was not uniformly dispersed and instead formed matrix-dependent C_{60}-rich domains. XRD and DSC analyses further showed that C_{60} affected each polymer differently: PHBV-C_{60} exhibited the most structurally stable response, PLA-C_{60} showed strong fullerene heterogeneity and reduced crystallinity, and chitosan-C_{60} showed phase-separated C_{60} domains and water-dependent thermal behaviour.

All C_{60}-containing films generated singlet oxygen under 450 nm blue-light irradiation, confirming that the fullerene retained its photodynamic activity after processing. PLA-C_{60} produced the highest ROS signal, followed by PHBV-C_{60} and chitosan-C_{60}. Microbiological assays confirmed the light-dependent antibacterial activity against surface-associated S. aureus. PLA-C_{60} was the most effective during bacterial attachment, whereas PHBV-C_{60} showed the strongest reduction in pre-attached cells. Chitosan-C_{60} remained photoactive but exhibited the weakest antibacterial performance.

Overall, the results demonstrate that thermophysically processed C_{60}-containing biopolymer films can function as light-activated antimicrobial surfaces. The effectiveness of these materials depends strongly on the polymer matrix, indicating that fullerene distribution, ROS generation, and bacterial interaction with the surface must be considered together when designing photoactive antimicrobial coatings.

References

Alekseeva, O. V., Bagrovskaya, N. A., & Noskov, A. V. (2018). Effect of C60 filling on structure and properties of composite films based on polystyrene. *Arabian Journal of Chemistry*, *11*(7), 1160–1164. https://doi.org/10.1016/j.arabjc.2014.09.008

Almatroudi, A. (2025). Biofilm Resilience: Molecular Mechanisms Driving Antibiotic Resistance in Clinical Contexts. *Biology*, *14*(2), 165. https://doi.org/10.3390/biology14020165

Amoako, K., Ukita, R., & Cook, K. E. (2025). Antifouling Zwitterionic Polymer Coatings for Blood-Bearing Medical Devices. *Langmuir*, *41*(5), 2994–3006. https://doi.org/10.1021/acs.langmuir.4c04532

Back, N., Cohen, I. R., Lajtha, A., Lambris, J. D., Paoletti, R., Kolosnjaj, J., Szwarc, H., & Moussa, F. (2007). Toxicity Studies of Fullerenes and Derivatives. In W. C. W. Chan (Ed.), *Bio-Applications of Nanoparticles* (Vol. 620, pp. 168–180). Springer. https://doi.org/10.1007/978-0-387-76713-0_13

Ballatore, M. B., Durantini, J., Gsponer, N. S., Suarez, M. B., Gervaldo, M., Otero, L., Spesia, M. B., Milanesio, M. E., & Durantini, E. N. (2015). Photodynamic Inactivation of Bacteria Using Novel Electrogenerated Porphyrin-Fullerene C_{60} Polymeric Films. *Environmental Science & Technology*, *49*(12), 7456–7463. https://doi.org/10.1021/acs.est.5b01407

Bäumler, W., Eckl, D., Holzmann, T., & Schneider-Brachert, W. (2022). Antimicrobial coatings for environmental surfaces in hospitals: A potential new pillar for prevention strategies in hygiene. *Critical Reviews in Microbiology*, *48*(5), 531–564. https://doi.org/10.1080/1040841X.2021.1991271

Bolshakova, O., Lebedev, V., Mikhailova, E., Zherebyateva, O., Aznabaeva, L., Burdakov, V., Kulvelis, Y., Yevlampieva, N., Mironov, A., Miroshnichenko, I., & Sarantseva, S. (2023). Fullerenes on a Nanodiamond Platform Demonstrate Antibacterial Activity with Low Cytotoxicity. *Pharmaceutics*, *15*(7), 1984. https://doi.org/10.3390/pharmaceutics15071984

Botta, L., Scaffaro, R., Ceraulo, M., & Gallo, G. (2014). Antimicrobial thermoplastic materials for biomedical applications prepared by melt processing. *AIP Conference Proceedings*, *1599*(1), 310–313. https://doi.org/10.1063/1.4876840

Bouhrour, N., Nibbering, P. H., & Bendali, F. (2024). Medical Device-Associated Biofilm Infections and Multidrug-Resistant Pathogens. *Pathogens*, *13*(5), 393. https://doi.org/10.3390/pathogens13050393

Buhl, S., Peter, J., Stich, A., Brückner, R., & Bulitta, C. (2020). Durability and stability of antimicrobial coated surfaces. *Current Directions in Biomedical Engineering*, *6*(3), 298–300. https://doi.org/10.1515/cdbme-2020-3076

Bunin, D. A., Martynov, A. G., Gvozdev, D. A., & Gorbunova, Y. G. (2023). Phthalocyanine aggregates in the photodynamic therapy: Dogmas, controversies, and future prospects. *Biophysical Reviews*, *15*(5), 983–998. https://doi.org/10.1007/s12551-023-01129-7

Cheung, G. Y. C., Bae, J. S., & Otto, M. (2021). Pathogenicity and virulence of Staphylococcus aureus. *Virulence*, *12*(1), 547–569. https://doi.org/10.1080/21505594.2021.1878688

Cloutier, M., Mantovani, D., & Rosei, F. (2015). Antibacterial Coatings: Challenges, Perspectives, and Opportunities. *Trends in Biotechnology*, *33*(11), 637–652. https://doi.org/10.1016/j.tibtech.2015.09.002

Correlo, V. M., Costa-Pinto, A. R., Sol, P., Covas, J. A., Bhattacharya, M., Neves, N. M., & Reis, R. L. (2010). Melt processing of chitosan-based fibers and fiber-mesh scaffolds for the engineering of connective tissues. *Macromolecular Bioscience*, *10*(12), 1495–1504. https://doi.org/10.1002/mabi.201000011

Correlo, V. M., Martins, A., Neves, N. M., & Reis, R. L. (2016). Processing of Biomedical Devices for Tissue Engineering and Regenerative Medicine Applications. In *Biomaterials from Nature for Advanced Devices and Therapies* (pp. 475–493). John Wiley & Sons, Ltd. https://doi.org/10.1002/9781119126218.ch25

Craft, K. M., Nguyen, J. M., Berg, L. J., & Townsend, S. D. (2019). Methicillin-resistant Staphylococcus aureus (MRSA): Antibiotic-resistance and the biofilm phenotype. *MedChemComm*, *10*(8), 1231–1241. https://doi.org/10.1039/c9md00044e

Dash, M., Chiellini, F., Ottenbrite, R. M., & Chiellini, E. (2011). Chitosan—A versatile semi-synthetic polymer in biomedical applications. *Progress in Polymer Science, Special Issue on Biomaterials*, *36*(8), 981–1014. https://doi.org/10.1016/j.progpolymsci.2011.02.001

De-la-Pinta, I., Cobos, M., Ibarretxe, J., Montoya, E., Eraso, E., Guraya, T., & Quindós, G. (2019). Effect of biomaterials hydrophobicity and roughness on biofilm development. *Journal of Materials Science: Materials in Medicine*, *30*(7), 77. https://doi.org/10.1007/s10856-019-6281-3

Donlan, R. M. (2002). Biofilms: Microbial Life on Surfaces. *Emerging Infectious Diseases*, *8*(9), 881–890. https://doi.org/10.3201/eid0809.020063

Dorner-Reisel, A., Ritter, U., Moje, J., Freiberger, E., & Scharff, P. (2022). Effect of fullerene C60 thermal and tribomechanical loading on Raman signals. *Diamond and Related Materials*, *126*, 109036. https://doi.org/10.1016/j.diamond.2022.109036

Dube, E. (2024). Antimicrobial Photodynamic Therapy: Self-Disinfecting Surfaces for Controlling Microbial Infections. *Microorganisms*, *12*(8), 1573. https://doi.org/10.3390/microorganisms12081573

Dusunceli, N., & Colak, O. U. (2008). Modelling effects of degree of crystallinity on mechanical behavior of semicrystalline polymers. *International Journal of Plasticity*, *24*(7), 1224–1242. https://doi.org/10.1016/j.ijplas.2007.09.003

El Moumen, A., Tarfaoui, M., & Lafdi, K. (2019). Additive manufacturing of polymer composites: Processing and modeling approaches. *Composites Part B: Engineering*, *171*, 166–182. https://doi.org/10.1016/j.compositesb.2019.04.029

Epure, V., Griffon, M., Pollet, E., & Avérous, L. (2011). Structure and properties of glycerol-plasticized chitosan obtained by mechanical kneading. *Carbohydrate Polymers*, *83*(2), 947–952. https://doi.org/10.1016/j.carbpol.2010.09.003

Escudero, A., Carrillo-Carrión, C., Carmen Castillejos, M., Romero-Ben, E., Rosales-Barrios, C., & Khiar, N. (2021). Photodynamic therapy: Photosensitizers and nanostructures. *Materials Chemistry Frontiers*, *5*(10), 3788–3812. https://doi.org/10.1039/D0QM00922A

Exner, M., Bhattacharya, S., Gebel, J., Goroncy-Bermes, P., Hartemann, P., Heeg, P., Ilschner, C., Kramer, A., Ling, M. L., Merkens, W., Oltmanns, P., Pitten, F., Rotter, M., Schmithausen, R. M., Sonntag, H.-G., Steinhauer, K., & Trautmann, M. (2020). Chemical disinfection in healthcare settings: Critical aspects for the development of global strategies. *GMS Hygiene and Infection Control*, *15*, Doc36. https://doi.org/10.3205/dgkh000371

Falke, S., Eravuchira, P., Materny, A., & Lienau, C. (2011). Raman spectroscopic identification of fullerene inclusions in polymer/fullerene blends. *Journal of Raman Spectroscopy*, *42*(10), 1897–1900. https://doi.org/10.1002/jrs.2966

Fawaz, J., & Mittal, V. (2014). Synthesis of Polymer Nanocomposites: Review of Various Techniques. In V. Mittal (Ed.), *Synthesis Techniques for Polymer Nanocomposites* (1st ed., pp. 1–30). Wiley. https://doi.org/10.1002/9783527670307.ch1

Flemming, H.-C., Wingender, J., Szewzyk, U., Steinberg, P., Rice, S. A., & Kjelleberg, S. (2016). Biofilms: An emergent form of bacterial life. *Nature Reviews Microbiology*, *14*(9), 563–575. https://doi.org/10.1038/nrmicro.2016.94

Gao, P., & Masato, D. (2024). The Effects of Nucleating Agents and Processing on the Crystallization and Mechanical Properties of Polylactic Acid: A Review. *Micromachines*, *15*(6), 776. https://doi.org/10.3390/mi15060776

Gon, S., Kumar, K.-N., Nüsslein, K., & Santore, M. M. (2012). How Bacteria Adhere to Brushy PEG Surfaces: Clinging to Flaws and Compressing the Brush. *Macromolecules*, *45*(20), 8373–8381. https://doi.org/10.1021/ma300981r

Gonçalves, A. S. C., Leitão, M. M., Fernandes, J. R., Saavedra, M. J., Pereira, C., Simões, M., & Borges, A. (2024). Photodynamic activation of phytochemical-antibiotic combinations for combatting Staphylococcus aureus from acute wound infections. *Journal of Photochemistry and Photobiology. B, Biology*, *258*, 112978. https://doi.org/10.1016/j.jphotobiol.2024.112978

Gonzalez, E., Renfige Rodriguez, M., Samntamarina, S., Macor, L. P., Otero, L. A., Durantini, A. M., Durantini, E. N., Durantini, J. E., & Heredia, D. A. (2023). Light-Activated Antibacterial Polymeric Surface Based on Porphycene. *ACS Applied Polymer Materials*, *5*(1), 943–956. https://doi.org/10.1021/acsapm.2c01890

González-Vázquez, R., Córdova-Espinoza, M. G., Escamilla-Gutiérrez, A., Herrera-Cuevas, M. D. R., González-Vázquez, R., Esquivel-Campos, A. L., López-Pelcastre, L., Torres-Cubillas, W., Mayorga-Reyes, L., Mendoza-Pérez, F., Gutiérrez-Nava, M. A., & Giono-Cerezo, S. (2024). Detection of mecA Genes in Hospital-Acquired MRSA and SOSA Strains Associated with Biofilm Formation. *Pathogens*, *13*(3), 212. https://doi.org/10.3390/pathogens13030212

Guo, J., Tao, Y., Du, Z., Zhang, S., Zheng, W., Wang, Z., Yi, Z., Gou, Y., & Tang, W. (2025). Stimuli-responsive antimicrobial polymer systems: From structural design to biomedical applications. *Giant*, *24*, 100366. https://doi.org/10.1016/j.giant.2025.100366

Hamblin, M. R. (2016). Antimicrobial photodynamic inactivation: A bright new technique to kill resistant microbes. *Current Opinion in Microbiology, Antimicrobials • Microbial Systems Biology*, *33*, 67–73. https://doi.org/10.1016/j.mib.2016.06.008

Hamblin, M. R. (2018). Fullerenes as Photosensitizers in Photodynamic Therapy: Pros and Cons. *Photochemical & Photobiological Sciences : Official Journal of the European Photochemistry Association and the European Society for Photobiology*, *17*(11), 1515–1533. https://doi.org/10.1039/c8pp00195b

Heredia, D. A., Durantini, A. M., Durantini, J. E., & Durantini, E. N. (2022). Fullerene C60 derivatives as antimicrobial photodynamic agents. *Journal of Photochemistry and Photobiology C: Photochemistry Reviews*, *51*, 100471. https://doi.org/10.1016/j.jphotochemrev.2021.100471

Hou, W., Shi, G., Wu, S., Mo, J., Shen, L., Zhang, X., & Zhu, Y. (2022). Application of Fullerenes as Photosensitizers for Antimicrobial Photodynamic Inactivation: A Review. *Frontiers in Microbiology*, *13*. https://doi.org/10.3389/fmicb.2022.957698

Hu, X., Huang, Y.-Y., Wang, Y., Wang, X., & Hamblin, M. R. (2018). Antimicrobial Photodynamic Therapy to Control Clinically Relevant Biofilm Infections. *Frontiers in Microbiology*, *9*, 1299. https://doi.org/10.3389/fmicb.2018.01299

Hussain, M., Khan, S. M., Shafiq, M., & Abbas, N. (2024). A review on PLA-based biodegradable materials for biomedical applications. *Giant*, *18*, 100261. https://doi.org/10.1016/j.giant.2024.100261

Ibrahim, M. I., Alsafadi, D., Alamry, K. A., & Hussein, M. A. (2021). Properties and Applications of Poly(3-hydroxybutyrate-co-3-hydroxyvalerate) Biocomposites. *Journal of Polymers and the Environment*, *29*(4), 1010–1030. https://doi.org/10.1007/s10924-020-01946-x

Janik, W., Wojtala, A., Pietruszka, A., Dudek, G., & Sabura, E. (2021). Environmentally Friendly Melt-Processed Chitosan/Starch Composites Modified with PVA and Lignin. *Polymers*, *13*(16), 2685. https://doi.org/10.3390/polym13162685

Jo, J., Price-Whelan, A., & Dietrich, L. E. P. (2022). Gradients and consequences of heterogeneity in biofilms. *Nature Reviews. Microbiology*, *20*(10), 593–607. https://doi.org/10.1038/s41579-022-00692-2

Kang, Y., Li, Z., Yang, Y., Su, Z., Ji, X., & Zhang, S. (2021). Antimonene Nanosheets-Based Z-Scheme Heterostructure with Enhanced Reactive Oxygen Species Generation and Photothermal Conversion Efficiency for Photonic Therapy of Cancer. *Advanced Healthcare Materials*, *10*(3), 2001835. https://doi.org/10.1002/adhm.202001835

Kaur, R., & Liu, S. (2016). Antibacterial surface design – Contact kill. *Progress in Surface Science*, *91*(3), 136–153. https://doi.org/10.1016/j.progsurf.2016.09.001

Klausen, M., Ucuncu, M., & Bradley, M. (2020). Design of Photosensitizing Agents for Targeted Antimicrobial Photodynamic Therapy. *Molecules*, *25*(22), 5239. https://doi.org/10.3390/molecules25225239

Kwiatkowski, S., Knap, B., Przystupski, D., Saczko, J., Kędzierska, E., Knap-Czop, K., Kotlińska, J., Michel, O., Kotowski, K., & Kulbacka, J. (2018). Photodynamic therapy—Mechanisms, photosensitizers and combinations. *Biomedicine & Pharmacotherapy = Biomedecine & Pharmacotherapie*, *106*, 1098–1107. https://doi.org/10.1016/j.biopha.2018.07.049

Leceta, I., Guerrero, P., & de la Caba, K. (2013). Functional properties of chitosan-based films. *Carbohydrate Polymers, 2nd European Polysaccharide Network of Excellence International Conference, August 2011*, *93*(1), 339–346. https://doi.org/10.1016/j.carbpol.2012.04.031

Ledwoch, K., Dancer, S. J., Otter, J. A., Kerr, K., Roposte, D., Rushton, L., Weiser, R., Mahenthiralingam, E., Muir, D. D., & Maillard, J.-Y. (2018). Beware biofilm! Dry biofilms containing bacterial pathogens on multiple healthcare surfaces; a multi-centre study. *Journal of Hospital Infection*, *100*(3), e47–e56. https://doi.org/10.1016/j.jhin.2018.06.028

Lee, J., Yamakoshi, Y., Hughes, J. B., & Kim, J.-H. (2008). Mechanism of C60 photoreactivity in water: Fate of triplet state and radical anion and production of reactive oxygen species. *Environmental Science & Technology*, *42*(9), 3459–3464. https://doi.org/10.1021/es702905g

Li, X., Kolemen, S., Yoon, J., & Akkaya, E. U. (2017). Activatable Photosensitizers: Agents for Selective Photodynamic Therapy. *Advanced Functional Materials*, *27*(5), 1604053. https://doi.org/10.1002/adfm.201604053

Li, Y., Sun, G., Xie, J., Xiao, S., & Lin, C. (2023). Antimicrobial photodynamic therapy against oral biofilm: Influencing factors, mechanisms, and combined actions with other strategies. *Frontiers in Microbiology*, *14*. https://doi.org/10.3389/fmicb.2023.1192955

Lindsay, D., & von Holy, A. (2006). Bacterial biofilms within the clinical setting: What healthcare professionals should know. *Journal of Hospital Infection*, *64*(4), 313–325. https://doi.org/10.1016/j.jhin.2006.06.028

Liu, S., Tang, J., Ji, F., Lin, W., & Chen, S. (2022). Recent Advances in Zwitterionic Hydrogels: Preparation, Property, and Biomedical Application. *Gels*, *8*(1), 46. https://doi.org/10.3390/gels8010046

Liu, Y., Chen, J., Li, P., & Ning, N. (2021). The Effect of Chitosan in Wound Healing: A Systematic Review. *Advances in Skin & Wound Care*, *34*(5), 262–266. https://doi.org/10.1097/01.ASW.0000723128.58588.b5

Maillard, J.-Y., & Centeleghe, I. (2023). How biofilm changes our understanding of cleaning and disinfection. *Antimicrobial Resistance & Infection Control*, *12*(1), 95. https://doi.org/10.1186/s13756-023-01290-4

Maillard, J.-Y., & Pascoe, M. (2024). Disinfectants and antiseptics: Mechanisms of action and resistance. *Nature Reviews Microbiology*, *22*(1), 4–17. https://doi.org/10.1038/s41579-023-00958-3

Matet, M., Heuzey, M.-C., Pollet, E., Ajji, A., & Avérous, L. (2013). Innovative thermoplastic chitosan obtained by thermo-mechanical mixing with polyol plasticizers. *Carbohydrate Polymers*, *95*(1), 241–251. https://doi.org/10.1016/j.carbpol.2013.02.052

McCluskey, D. M., Smith, T. N., Madasu, P. K., Coumbe, C. E., Mackey, M. A., Fulmer, P. A., Wynne, J. H., Stevenson, S., & Phillips, J. P. (2009). Evidence for Singlet-Oxygen Generation and Biocidal Activity in Photoresponsive Metallic Nitride Fullerene−Polymer Adhesive Films. *ACS Applied Materials & Interfaces*, *1*(4), 882–887. https://doi.org/10.1021/am900008v

Merijs-Meri, R., Zicans, J., Ivanova, T., Mezule, L., Ivanickins, A., Bockovs, I., Bitenieks, J., Berzina, R., & Lebedeva, A. (2024). Melt-Processed Polybutylene-Succinate Biocomposites with Chitosan: Development and Characterization of Rheological, Thermal, Mechanical and Antimicrobial Properties. *Polymers*, *16*(19), 2808. https://doi.org/10.3390/polym16192808

Moayedi, S., Xia, W., Lundergan, L., Yuan, H., & Xu, J. (2024). Zwitterionic Polymers for Biomedical Applications: Antimicrobial and Antifouling Strategies toward Implantable Medical Devices and Drug Delivery. *Langmuir*, *40*(44), 23125–23145. https://doi.org/10.1021/acs.langmuir.4c02664

Moll, E., & Chiralt, A. (2026). Biodegradable and active materials based on PHBV for sustainable food packaging. *Sustainable Food Technology*. https://doi.org/10.1039/D5FB00936G

Moneira, M. L., Lyon, P., J., Romani Paula, A., Severino, D., Maira Regina, M., & De Oliveir, H. P. M. (2012). Phenotiazinium Dyes as Photosensitizers (PS) in Photodynamic Therapy (PDT): Spectroscopic Properties and Photochemical Mechanisms. In M. Akhyar Farrukh (Ed.), *Advanced Aspects of Spectroscopy*. InTech. https://doi.org/10.5772/48087

Mroz, P., Tegos, G. P., Gali, H., Wharton, T., Sarna, T., & Hamblin, M. R. (2007). Photodynamic therapy with fullerenes. *Photochemical & Photobiological Sciences : Official Journal of the European Photochemistry Association and the European Society for Photobiology*, *6*(11), 1139–1149. https://doi.org/10.1039/b711141j

Mu, M., Wang, X., Taylor, M., Castillo, A., Cisneros-Zevallos, L., Akbulut, M., & Min, Y. (2023). Multifunctional coatings for mitigating bacterial fouling and contamination. *Colloid and Interface Science Communications*, *55*, 100717. https://doi.org/10.1016/j.colcom.2023.100717

Navarro, M., Ginebra, M. P., Planell, J. A., Zeppetelli, S., & Ambrosio, L. (2004). Development and cell response of a new biodegradable composite scaffold for guided bone regeneration. *Journal of Materials Science: Materials in Medicine*, *15*(4), 419–422. https://doi.org/10.1023/B:JMSM.0000021113.88702.9d

Naves, P., Del Prado, G., Ponte, C., & Soriano, F. (2010). Differences in the In Vitro Susceptibility of Planktonic and Biofilm-Associated Escherichia Coli Strains to Antimicrobial Agents. *Journal of Chemotherapy*, *22*(5), 312–317. https://doi.org/10.1179/joc.2010.22.5.312

Nikonova, R., Lad'yanov, V., Rekhviashvili, S., & Pskhu, A. (2021). Thermal Stability of C60 and C70 Fullerites. *High Temperature*, *59*, 179–183. https://doi.org/10.1134/S0018151X21020103

Nnaji, N. D., Anyanwu, C. U., Miri, T., & Onyeaka, H. (2024). Mechanisms of Heavy Metal Tolerance in Bacteria: A Review. *Sustainability*, *16*(24), 11124. https://doi.org/10.3390/su162411124

Nyga, A., Blacha-Grzechnik, A., Podsiadły, P., Duda, A., Kępska, K., Krzywiecki, M., Motyka, R., Janssen, R. A. J., & Data, P. (2022). Singlet oxygen formation from photoexcited P3HT:PCBM films applied in oxidation reactions. *Materials Advances*, *3*(4), 2063–2069. https://doi.org/10.1039/D1MA01151K

Odoyo, E., Matano, D., Tiria, F., Georges, M., Kyanya, C., Wahome, S., Mutai, W., & Musila, L. (2023). Environmental contamination across multiple hospital departments with multidrug-resistant bacteria pose an elevated risk of healthcare-associated infections in Kenyan hospitals. *Antimicrobial Resistance & Infection Control*, *12*(1), 22. https://doi.org/10.1186/s13756-023-01227-x

Otter, J. A., Vickery, K., Walker, J. T., Pulcini, E. deLancey, Stoodley, P., Goldenberg, S. D., Salkeld, J. a. G., Chewins, J., Yezli, S., & Edgeworth, J. D. (2015). Surface-attached cells, biofilms and biocide susceptibility: Implications for hospital cleaning and disinfection. *Journal of Hospital Infection*, *89*(1), 16–27. https://doi.org/10.1016/j.jhin.2014.09.008

Otto, M. (2018). Staphylococcal Biofilms. *Microbiology Spectrum*, *6*(4), 10.1128/microbiolspec.gpp3-0023–2018. https://doi.org/10.1128/microbiolspec.gpp3-0023-2018

Pallós, P., Gajdács, M., Urbán, E., Szabados, Y., Szalai, K., Hevesi, L., Horváth, A., Kuklis, A., Morjaria, D., Iffat, W., Hetta, H. F., Piredda, N., & Donadu, M. G. (2024). Characterization of antibiotic and disinfectant susceptibility in biofilm-forming Acinetobacter baumannii: A focus on environmental isolates. *European Journal of Microbiology and Immunology*, *14*(2), 126–133. https://doi.org/10.1556/1886.2024.00014

Pan, Y., Liu, X., Zhang, W., Liu, Z., Zeng, G., Shao, B., Liang, Q., He, Q., Yuan, X., Huang, D., & Chen, M. (2020). Advances in photocatalysis based on fullerene C60 and its derivatives: Properties, mechanism, synthesis, and applications. *Applied Catalysis B: Environmental*, *265*, 118579. https://doi.org/10.1016/j.apcatb.2019.118579

Penkova, A. V., Acquah, S. F., Piotrovskiy, L. B., Markelov, D. A., Semisalova, A. S., & Kroto, H. W. (2017). Fullerene derivatives as nano-additives in polymer composites. *Russian Chemical Reviews*, *86*(6), 530–566. https://doi.org/10.1070/RCR4712

Pereira, P., Fernandes, L., Gaspar, H., & Bernardo, G. (2015). Melt processed polyethylene/fullerene nanocomposites with highly improved thermo-oxidative stability. *Polymer Testing*, *45*, 124–131. https://doi.org/10.1016/j.polymertesting.2015.06.002

Pereira-Silva, P., Borges, J., & Sampaio, P. (2025). Recent advances in metal-based antimicrobial coatings. *Advances in Colloid and Interface Science*, *344*, 103590. https://doi.org/10.1016/j.cis.2025.103590

Phillips, J. P., Deng, X., Todd, M. L., Heaps, D. T., Stevenson, S., Zhou, H., & Hoyle, C. E. (2008). Singlet oxygen generation and adhesive loss in stimuli-responsive, fullerene-polymer blends, containing polystyrene-block-polybutadiene-block-polystyrene and polystyrene-block-polyisoprene-block-polystyrene rubber-based adhesives. *Journal of Applied Polymer Science*, *109*(5), 2895–2904. https://doi.org/10.1002/app.28337

Pinto, R. M., Soares, F. A., Reis, S., Nunes, C., & Van Dijck, P. (2020). Innovative Strategies Toward the Disassembly of the EPS Matrix in Bacterial Biofilms. *Frontiers in Microbiology*, *11*. https://doi.org/10.3389/fmicb.2020.00952

Point prevalence survey of healthcare-associated infections and antimicrobial use in European acute care hospitals – 2022-2023. (2024). European Centre for Disease Prevention and Control. https://www.ecdc.europa.eu/en/publications-data/PPS-HAI-AMR-acute-care-europe-2022-2023

Prylutskyy, Y. I., Buchelnikov, A. S., Voronin, D. P., Kostjukov, V. V., Ritter, U., Parkinson, J. A., & Evstigneev, M. P. (2013). C60 fullerene aggregation in aqueous solution. *Physical Chemistry Chemical Physics: PCCP*, *15*(23), 9351–9360. https://doi.org/10.1039/c3cp50187f

Pucelik, B., Barzowska, A., Sułek, A., Werłos, M., & Dąbrowski, J. M. (2024). Refining antimicrobial photodynamic therapy: Effect of charge distribution and central metal ion in fluorinated porphyrins on effective control of planktonic and biofilm bacterial forms. *Photochemical & Photobiological Sciences*, *23*(3), 539–560. https://doi.org/10.1007/s43630-024-00538-1

Qin, Y., Xu, J., Liang, Z., Teng, H., Zhan, D., & Xu, H. (2025). Raman Spectroscopy of Fullerenes: From C60 to Functionalized Derivatives. *Molecules*, *30*(3), 738. https://doi.org/10.3390/molecules30030738

Quinones, M., Zhang, Y., Riascos, P., Hwang, H.-M., Aker, W. G., He, X., & Gao, R. (2014). Effects of Light Energy and Reducing Agents on C60-Mediated Photosensitizing Reactions. *Photochemistry and Photobiology*, *90*(2), 374–379. https://doi.org/10.1111/php.12206

Rapacka-Zdończyk, A., Woźniak, A., Michalska, K., Pierański, M., Ogonowska, P., Grinholc, M., & Nakonieczna, J. (2021). Factors Determining the Susceptibility of Bacteria to Antibacterial Photodynamic Inactivation. *Frontiers in Medicine*, *8*. https://doi.org/10.3389/fmed.2021.642609

Rapacka-Zdonczyk, A., Wozniak, A., Nakonieczna, J., & Grinholc, M. (2021). Development of Antimicrobial Phototreatment Tolerance: Why the Methodology Matters. *International Journal of Molecular Sciences*, *22*(4), 2224. https://doi.org/10.3390/ijms22042224

Reynoso, E., Durantini, A. M., Solis, C. A., Macor, L. P., Otero, L. A., Gervaldo, M. A., Durantini, E. N., & Heredia, D. A. (2021). Photoactive antimicrobial coating based on a PEDOT-fullerene C60 polymeric dyad. *RSC Advances*, *11*(38), 23519–23532. https://doi.org/10.1039/D1RA03417K

Reynoso, E., Ferreyra, D. D., Durantini, E. N., & Spesia, M. B. (2019). Photodynamic inactivation to prevent and disrupt Staphylococcus aureus biofilm under different media conditions. *Photodermatology, Photoimmunology & Photomedicine*, *35*(5), 322–331. https://doi.org/10.1111/phpp.12477

Rondags, A., Yuen, W. Y., Jonkman, M. F., & Horváth, B. (2017). Fullerene C60 with cytoprotective and cytotoxic potential: Prospects as a novel treatment agent in Dermatology? *Experimental Dermatology*, *26*(3), 220–224. https://doi.org/10.1111/exd.13172

Samia, N. I., Robicsek, A., Heesterbeek, H., & Peterson, L. R. (2022). Methicillin-resistant staphylococcus aureus nosocomial infection has a distinct epidemiological position and acts as a marker for overall hospital-acquired infection trends. *Scientific Reports*, *12*(1), 17007. https://doi.org/10.1038/s41598-022-21300-6

Samoilova, N. A., Krayukhina, M. A., Klemenkova, Z. S., Naumkin, A. V., Buzin, M. I., Mezhuev, Y. O., Turetsky, E. A., Andreev, S. M., Anuchina, N. M., & Popov, D. A. (2024). Hydrophilization and Functionalization of Fullerene C60 with Maleic Acid Copolymers by Forming a Non-Covalent Complex. *Polymers*, *16*(12), 1736. https://doi.org/10.3390/polym16121736

Santoro, O., & Izzo, L. (2024). Antimicrobial Polymer Surfaces Containing Quaternary Ammonium Centers (QACs): Synthesis and Mechanism of Action. *International Journal of Molecular Sciences*, *25*(14), 7587. https://doi.org/10.3390/ijms25147587

Sauer, K., Stoodley, P., Goeres, D. M., Hall-Stoodley, L., Burmølle, M., Stewart, P. S., & Bjarnsholt, T. (2023). The biofilm life cycle– expanding the conceptual model of biofilm formation. *Nature Reviews. Microbiology*, *20*(10), 608–620. https://doi.org/10.1038/s41579-022-00767-0

Saulėnienė, G., Kirsnyte-Snioke, M., Stirkė, A., Jasulaitiene, V., Straksys, A., Dobilaitis, S., & Melo, W. C. M. A. (2024). Development of photoactive biomaterial using modified fullerene nanoparticles. *Frontiers in Chemistry*, *12*. https://doi.org/10.3389/fchem.2024.1432624

Savagatrup, S., Makaram, A. S., Burke, D. J., & Lipomi, D. J. (2014). Mechanical Properties of Conjugated Polymers and Polymer-Fullerene Composites as a Function of Molecular Structure. *Advanced Functional Materials*, *24*(16), 2264–2264. https://doi.org/10.1002/adfm.201400595

Sharma, S., Mohler, J., Mahajan, S. D., Schwartz, S. A., Bruggemann, L., & Aalinkeel, R. (2023). Microbial Biofilm: A Review on Formation, Infection, Antibiotic Resistance, Control Measures, and Innovative Treatment. *Microorganisms*, *11*(6), 1614. https://doi.org/10.3390/microorganisms11061614

Soon, Y. W., Cho, H., Low, J., Bronstein, H., McCulloch, I., & Durrant, J. R. (2013). Correlating triplet yield, singlet oxygen generation and photochemical stability in polymer/fullerene blend films. *Chemical Communications*, *49*(13), 1291–1293. https://doi.org/10.1039/C2CC38243A

Spagnul, C., Turner, L. C., & Boyle, R. W. (2015). Immobilized photosensitizers for antimicrobial applications. *Journal of Photochemistry and Photobiology B: Biology, SI:Photoantimicrobials*, *150*, 11–30. https://doi.org/10.1016/j.jphotobiol.2015.04.021

Speller, E. M., McGettrick, J. D., Rice, B., Telford, A. M., Lee, H. K. H., Tan, C.-H., De Castro, C. S., Davies, M. L., Watson, T. M., Nelson, J., Durrant, J. R., Li, Z., & Tsoi, W. C. (2017). Impact of Aggregation on the Photochemistry of Fullerene Films: Correlating Stability to Triplet Exciton Kinetics. *ACS Applied Materials & Interfaces*, *9*(27), 22739–22747. https://doi.org/10.1021/acsami.7b03298

Steinbeck, M. J., Khan, A. U., & Karnovsky, M. J. (1992). Intracellular singlet oxygen generation by phagocytosing neutrophils in response to particles coated with a chemical trap. *Journal of Biological Chemistry*, *267*(19), 13425–13433. https://doi.org/10.1016/S0021-9258(18)42228-4

Sultana Phd Ceng Csci, N., & Wang, M. (2011). PHBV Tissue Engineering Scaffolds Fabricated via Emulsion Freezing / Freeze-drying: Effects of Processing Parameters. *IPCBEE*, *11*.

Tang, Z., Zhang, C., Liu, X., & Zhu, J. (2012). The crystallization behavior and mechanical properties of polylactic acid in the presence of a crystal nucleating agent. *Journal of Applied Polymer Science*, *125*(2), 1108–1115. https://doi.org/10.1002/app.34799

Tao, Y., Zhang, Y., Xia, T., & Lin, N. (2024). Melt Compounding of Poly(lactic acid)-Based Composites: Blending Strategies, Process Conditions, and Mechanical Properties. *Macromolecular Rapid Communications*, *45*(20), 2400380. https://doi.org/10.1002/marc.202400380

Tegos, G. P., Demidova, T. N., Arcila-Lopez, D., Lee, H., Wharton, T., Gali, H., & Hamblin, M. R. (2005). Cationic Fullerenes Are Effective and Selective Antimicrobial Photosensitizers. *Chemistry & Biology*, *12*(10), 1127–1135. https://doi.org/10.1016/j.chembiol.2005.08.014

Todorić, O., Pezo, L., Šarić, L., Kolarov, V., Varga, A., Čabarkapa, I., & Kocić-Tanackov, S. (2023). Comparison of the Efficiency of Selected Disinfectants against Planktonic and Biofilm Populations of Escherichia coli and Staphylococcus aureus. *Microorganisms*, *11*(6), 1593. https://doi.org/10.3390/microorganisms11061593

Tolker-Nielsen, T. (2015). Biofilm Development. In *Microbial Biofilms, Second Edition* (pp. 51–66). ASM Press. https://doi.org/10.1128/9781555817466.ch3

Tomić, S. L., & Vuković, J. S. (2022). Antimicrobial Activity of Silver, Copper, and Zinc Ions/Poly(Acrylate/Itaconic Acid) Hydrogel Matrices. *Inorganics*, *10*(3), 38. https://doi.org/10.3390/inorganics10030038

Tong, S. Y. C., Davis, J. S., Eichenberger, E., Holland, T. L., & Fowler, V. G. (2015). Staphylococcus aureus Infections: Epidemiology, Pathophysiology, Clinical Manifestations, and Management. *Clinical Microbiology Reviews*, *28*(3), 603–661. https://doi.org/10.1128/CMR.00134-14

Tóth, L. F., Sukumaran, J., Szebényi, G., & De Baets, P. (2019). Tribo-mechanical interpretation for advanced thermoplastics and the effects of wear-induced crystallization. *Wear*, *440–441*, 203083. https://doi.org/10.1016/j.wear.2019.203083

Tran, L. C., Su, X., Nguyen, H., La, L. B. T., Adu, P., Jia, Q., Lee, I., Kuan, H.-C., Liu, X., & Ma, J. (2025). Advancing polymer nanocomposites through mechanochemical approaches. *Advanced Nanocomposites*, *2*, 86–107. https://doi.org/10.1016/j.adna.2025.03.002

Ul Haq, I., Khan, T. A., & Krukiewicz, K. (2024). Etiology, pathology, and host-impaired immunity in medical implant-associated infections. *Journal of Infection and Public Health*, *17*(2), 189–203. https://doi.org/10.1016/j.jiph.2023.11.024

Uneputty, A., Dávila-Lezama, A., Garibo, D., Oknianska, A., Bogdanchikova, N., Hernández-Sánchez, J. F., & Susarrey-Arce, A. (2022). Strategies applied to modify structured and smooth surfaces: A step closer to reduce bacterial adhesion and biofilm formation. *Colloid and Interface Science Communications*, *46*, 100560. https://doi.org/10.1016/j.colcom.2021.100560

Velghe, I., Buffel, B., Vandeginste, V., Thielemans, W., & Desplentere, F. (2023). Review on the Degradation of Poly(lactic acid) during Melt Processing. *Polymers*, *15*(9), 2047. https://doi.org/10.3390/polym15092047

Wang, D., Zhao, J., Mulder, R. J., Ratcliffe, J., Wang, C., Wu, B., Wang, J., & Hao, X. (2023). Highly aqueously stable C60-polymer nanoparticles with excellent photodynamic property for potential cancer treatment. *Smart Medicine*, *2*(4), e20230033. https://doi.org/10.1002/SMMD.20230033

Wang, X., Liu, M., Yu, C., Li, J., & Zhou, X. (2023). Biofilm formation: Mechanistic insights and therapeutic targets. *Molecular Biomedicine*, *4*, 49. https://doi.org/10.1186/s43556-023-00164-w

Wang, X., Shan, M., Zhang, S., Chen, X., Liu, W., Chen, J., & Liu, X. (2022). Stimuli-Responsive Antibacterial Materials: Molecular Structures, Design Principles, and Biomedical Applications. *Advanced Science*, *9*(13), 2104843. https://doi.org/10.1002/advs.202104843

Wang, X., Zhu, L., Gu, Z., & Dai, L. (2022). Carbon nanomaterials for phototherapy. *Nanophotonics*, *11*(22), 4955–4976. https://doi.org/10.1515/nanoph-2022-0574

Wilkinson, D., Váchová, L., & Palková, Z. (2025). Hostile Environments: Modifying Surfaces to Block Microbial Adhesion and Biofilm Formation. *Biomolecules*, *15*(6), 754. https://doi.org/10.3390/biom15060754

Wylie, M. P., Irwin, N. J., Howard, D., Heydon, K., & McCoy, C. P. (2021). Hot-melt extrusion of photodynamic antimicrobial polymers for prevention of microbial contamination. *Journal of Photochemistry and Photobiology B: Biology*, *214*, 112098. https://doi.org/10.1016/j.jphotobiol.2020.112098

Yadav, H., Malviya, R., & Kaushik, N. (2024). Chitosan in biomedicine: A comprehensive review of recent developments. *Carbohydrate Polymer Technologies and Applications*, *8*, 100551. https://doi.org/10.1016/j.carpta.2024.100551

Yang, Y., Cai, Z., Huang, Z., Tang, X., & Zhang, X. (2018). Antimicrobial cationic polymers: From structural design to functional control. *Polymer Journal*, *50*(1), 33–44. https://doi.org/10.1038/pj.2017.72

Yao, M., Cui, W., Xiao, J., Chen, S., Cui, J., Liu, R., Cui, T., Zou, B., Liu, B., & Sundqvist, B. (2013). Pressure-induced transformation and superhard phase in fullerenes: The effect of solvent intercalation. *Applied Physics Letters*, *103*(7), 071913. https://doi.org/10.1063/1.4818909

Yun-Chong, F., & Yun-Fan, J. (2010). Molecular vibration spectroscopy study of irradiation effect in C60 films induced by low energy ion. *Journal of Applied Physics*, *108*(10), 104909. https://doi.org/10.1063/1.3512968

Zembouai, I., Kaci, M., Bruzaud, S., Benhamida, A., Corre, Y.-M., & Grohens, Y. (2013). A study of morphological, thermal, rheological and barrier properties of Poly(3-hydroxybutyrate-Co-3-Hydroxyvalerate)/polylactide blends prepared by melt mixing. *Polymer Testing*, *32*(5), 842–851. https://doi.org/10.1016/j.polymertesting.2013.04.004

Zhang, P., Sun, F., Liu, S., & Jiang, S. (2016). Anti-PEG antibodies in the clinic: Current issues and beyond PEGylation. *Journal of Controlled Release : Official Journal of the Controlled Release Society*, *244*(Pt B), 184–193. https://doi.org/10.1016/j.jconrel.2016.06.040

Zhang, T., Liu, Q., Meng, F., Hou, Y., Leung, M. K. H., Wen, Y., & Zhang, Q. (2024). Recent advances in stimuli-responsive antibacterial coatings: Bacteria-killing and releasing mechanism, design strategies, and potential applications. *Progress in Organic Coatings*, *186*, 107923. https://doi.org/10.1016/j.porgcoat.2023.107923

Z. Naser, A., Deiab, I., & M. Darras, B. (2021). Poly(lactic acid) (PLA) and polyhydroxyalkanoates (PHAs), green alternatives to petroleum-based plastics: A review. *RSC Advances*, *11*(28), 17151–17196. https://doi.org/10.1039/D1RA02390J

Appendixes

Appendix A

Supplementary DSC Data

Table A1. DSC thermal parameters of PLA, PLA–C60, PHBV, and PHBV–C60 films

Sample	Tg / relaxation peak (°C)	ΔH_relax (J/g)	Tcc (°C)	ΔHcc (J/g)	Treorg (°C)	ΔHreorg (J/g)	Tm1 (°C)	ΔHm1 (J/g)	Tm2 (°C)	ΔHm2 (J/g)	Tm3 (°C)	ΔHm3 (J/g)	ΔHm,total (J/g)	Xc (%)
Neat PLA	59.19	0.613	-	-	112.24	0.236	141.28	0.254	151.96	1.805	160.46	0.268	2.327	2.25
PLA–C60	55.5	0.696	105	2.409	112.57	0.1617	144.61	1.266	153.96	1.655	-	-	2.921	0.58
Neat PHBV	-	-	-	-	-	-	142.57	4.757	155.2	3.807	-	-	8.565	5.84
PHBV–C60	-	-	-	-	-	-	148.39	4.625	156.99	4.303	167.09	0.388	9.316	6.69

Note. Note: Enthalpy values were obtained from integrated peak areas after baseline correction in OriginPro 2026. "–" indicates the absence of a clearly defined peak.

Table A2. DSC thermal events of chitosan and chitosan–C60 films

Sample	Trelax (°C)	ΔHrelax (J/g)	Tdehydration (°C)	ΔHdehydration (J/g)
Neat Chitosan	67.99	2.688	109.52	33.733
Chitosan – C60	85.25	7.865	123.05	33.393

Note. Enthalpy values were obtained from integrated peak areas after baseline correction in OriginPro 2026. "–" indicates that no clearly defined peak was detected

Appendix B

SEM images

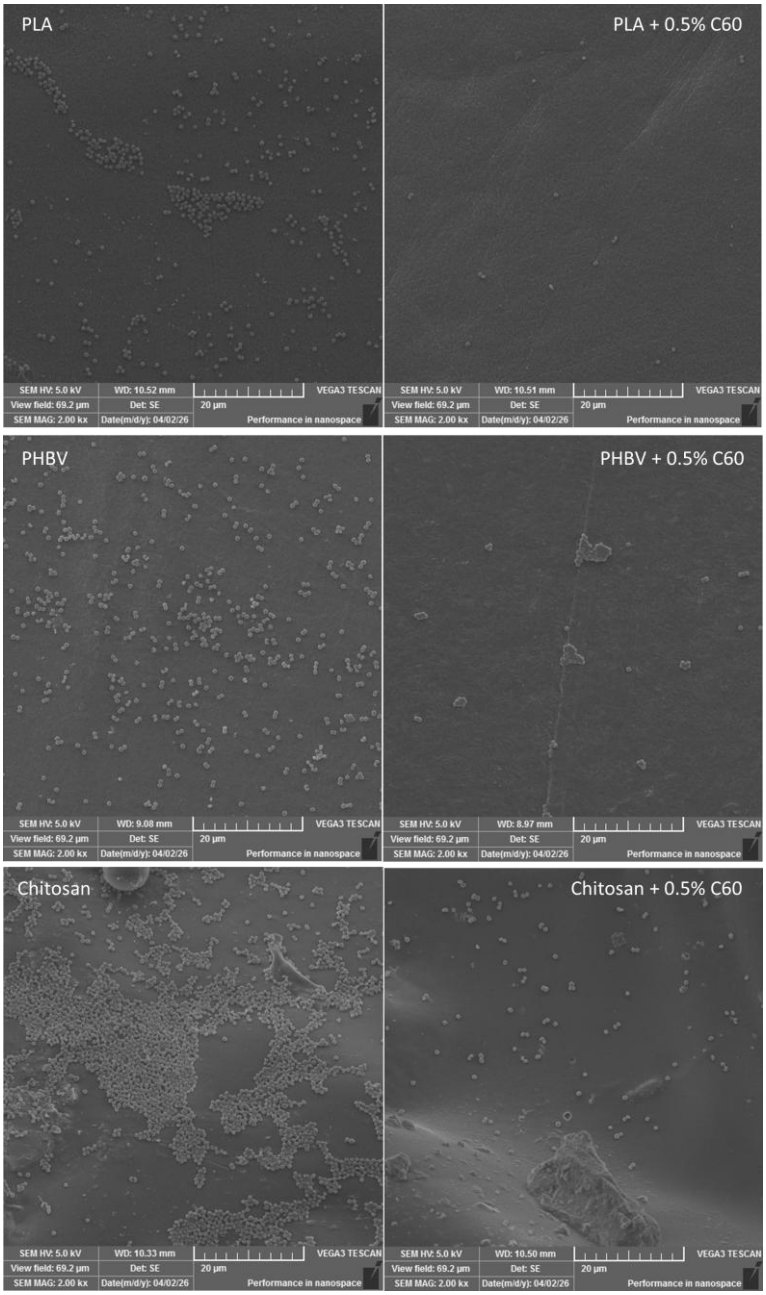

Figure B1. SEM micrographs of S. aureus on neat and 0.5% C60-containing PLA, PHBV, and chitosan films after 90 min of bacterial attachment, 2 h of blue-light exposure, washing, fixation, dehydration, and Ta sputter coating. All samples were processed under identical conditions. Images were acquired using SE detection at 2.00 kx magnification. Scale bar = 20